Journal of Industrial and Engineering Chemistry 153 (2026) 742–758

Contents lists available at ScienceDirect

Journal of Industrial and Engineering Chemistry

journal homepage: www.elsevier.com/locate/jiec

Full Length Article

Structural and luminescence properties of Tb^{3+}-doped $Na_2Gd_2B_2O_7$ phosphors for LED applications: Judd–Ofelt analysis and alkali co-doping effects

G. Souadi [a], M.B. Coban [b], U.H. Kaynar [c,d], H. Aydin [e,f], S.Cam Kaynar [g], V. Onar [h], A. Canimoglu [i], Hussain J Alathlawi [a], N. Can [a,j,*]

[a] Jazan University, College of Science, Department of Physical Sciences, Physics Division, P.O. Box 114, Jazan 45142, Saudi Arabia
[b] Balikesir University, Faculty of Arts and Sciences, Department of Physics, Balikesir, Turkey
[c] Bakırcay University, Faculty of Engineering and Architecture, Department of Fundamental Sciences, Menemen, Izmir, Turkey
[d] Bakırcay University, Biomedical Technologies Design Application and Research Center, Menemen, Izmir, Turkey
[e] Central Research Laboratories, Izmir Katip Celebi University, Izmir, Turkey
[f] Graphene Application&Research Center, Izmir Katip Celebi University, Izmir, Turkey
[g] Manisa Celal Bayar University, Faculty of Engineering and Natural Sciences, Physics Department, Manisa, Turkiye
[h] Mechanical Engineering Department, Faculty of Technology, Pamukkale University, Kinikli, Denizli, Turkey
[i] Nigde Omer Halisdemir University, Faculty of Science, Physics Department, Nigde, Turkey
[j] Nanotechnology Research Unit, College of Science, Jazan University, P.O. Box. 114, Jazan 45142, Saudi Arabia

ARTICLE INFO

Keywords:
$Na_2Gd_2B_2O_7$ phosphors
Tb^{3+} doping
Alkali ion co-doping
Photoluminescence
Judd–Ofelt analysis
Negative thermal quenching (NTQ)
Solid-state lighting

ABSTRACT

In this study, we report the structural and luminescent properties of Tb^{3+}-activated $Na_2Gd_2B_2O_7$ (NGBO) phosphors synthesized via a microwave-assisted gel combustion method. The effect of alkali ion co-doping (K^+, Li^+) on emission efficiency, crystal structure, and color purity was systematically investigated under near-UV excitation (λ_{ex} = 377 nm). X-ray diffraction confirmed the formation of a single-phase monoclinic structure, while Fourier-transform infrared (FTIR) spectroscopy and Raman spectra revealed preserved BO_3/BO_4 units with minor vibrational shifts. The NGBO:0.02 Tb^{3+} sample showed strong green emission at 542 nm ($^5D_4 \rightarrow {}^7F_5$), with the highest intensity at 2 wt% Tb^{3+}, prior to concentration quenching. Judd–Ofelt (J-O) analysis gave $\Omega_4 = 0.41 \times 10^{-20}$ cm^2 and $\Omega_6 = 0.64 \times 10^{-20}$ cm^2, indicating favorable asymmetric environments. Notably, temperature-dependent PL studies exhibited negative thermal quenching up to 500 K, attributed to thermally released trapped carriers. Time-resolved photoluminescence (PL) revealed lifetimes up to 1.27 ms, enhanced by alkali doping due to reduced non-radiative losses. Co-doped samples showed tunable Commission Internationale de l'Éclairage (CIE) coordinates (x = 0.2728–0.3110, y = 0.3061–0.4508), approaching white-light emission. These results position NGBO:Tb^{3+} as a promising, thermally stable phosphor for solid-state lighting and optical sensing.

Introduction

The rapid advancement of solid-state lighting technologies has intensified the demand for rare-earth-doped phosphors with high emission efficiency, excellent thermal stability, and strong compatibility with near-ultraviolet (n-UV) excitation sources. Among rare-earth doped candidates, Tb^{3+}-activated green-emitting phosphors are particularly attractive due to their sharp and efficient $^5D_4 \rightarrow {}^7F_j$ transitions. Conventional hosts such as YBO_3:Tb^{3+} [1], $LaPO_4$:Tb^{3+} [2], and $SrAl_2O_4$:Tb^{3+} [3] have been extensively investigated for use in lighting and display technologies. These materials typically exhibit strong green emission under UV excitation, making them suitable for applications ranging from cathode ray tubes to fluorescent lamps.

In recent years, oxide-based phosphors have attracted growing interest due to their superior chemical and thermal stability, particularly in persistent and laser-based luminescence applications. For example, Fan et al. [4] demonstrated the successful synthesis of Tb^{3+}, Pr^{3+}, and Dy^{3+} monodoped $CaTa_4O_{11}$ phosphors via a molten salt method, achieving notable persistent luminescence lifetimes and thermal trap depth control, highlighting their utility in anti-counterfeiting and light

* Corresponding author at: Jazan University, College of Science, Department of Physical Sciences, Physics Division, P.O. Box 114, Jazan 45142, Saudi Arabia.
E-mail address: ncan@jazanu.edu.sa (N. Can).

https://doi.org/10.1016/j.jiec.2025.07.037
Received 12 June 2025; Received in revised form 7 July 2025; Accepted 15 July 2025
Available online 17 July 2025

storage. Meanwhile, Cui et al. [5] synthesized Er^{3+}/Yb^{3+} co-doped $BiTa_7O_{19}$ phosphors exhibiting extremely intense green up-conversion luminescence and a high absolute temperature sensitivity of 0.01624 K^{-1} at 475 K, highlighting their potential for applications in biological imaging and optical temperature sensing. These studies underscore the versatility of rare-earth doped oxide hosts and motivate the exploration of alternative matrices like NGBO for tunable and thermally robust photonic materials.

However, these traditional phosphor systems often suffer from intrinsic limitations under direct n-UV excitation, mainly due to the parity-forbidden nature of 4f–4f transitions in Tb^{3+}, resulting in low absorption cross-sections [6]. Moreover, issues related to phase instability, limited thermal endurance, or particle agglomeration in nanoscale formulations can hinder their integration into modern optoelectronic applications [2].

To address these limitations, researchers have increasingly focused on borate-based host materials, which offer high chemical and thermal stability, large bandgaps, and low phonon energies, making them ideal for rare-earth ion doping. Among these, NGBO has recently emerged as a promising candidate. Srivastava et al. [7] first demonstrated that co-doping NGBO with Ce^{3+} and Tb^{3+} ions enables efficient energy transfer, leading to enhanced green emission. Building on this, Guo et al. [6] achieved energy transfer efficiencies exceeding 80 % from Ce^{3+} to Tb^{3+}, validating the photoluminescent potential of this host. Separately, Sakthivel et al. [8] provided a comprehensive photoluminescence investigation of Eu^{3+}-doped $Na_2Gd_2B_2O_7$, revealing its structural robustness, sharp $^5D^0 \rightarrow {}^7F_2$ emissions peaking at ~ 621 nm, and outstanding color purity (~99 %) under n-UV excitation. Notably, the optimized composition NGBO:0.35Eu^{3+} demonstrated a high internal quantum efficiency of 70.8 %, excellent thermal stability (maintaining ~ 56 % emission at 150 °C), and compatibility with White Light-Emitting Diode (WLED) fabrication. These results firmly establish the NGBO host as a versatile platform for rare-earth doping, not only in the red spectral region but also as a chemically stable matrix for broader photonic applications. Despite these advances, most prior studies have relied on sensitizer-mediated mechanisms such as $Ce^{3+} \rightarrow Tb^{3+}$ transfer to boost Tb^{3+} excitation efficiency. While effective, such strategies add compositional complexity and may introduce instability under prolonged UV exposure. Nevertheless, the direct excitation mechanism and intrinsic photoluminescence behavior of Tb^{3+}-only doped NGBO remain poorly understood. This gap limits the rational design of simpler and more robust phosphor compositions suitable for scalable Light-Emitting Diode (LED) integration. To further tailor the photoluminescence properties, alkali ions such as K^+ and Li^+ were introduced to modulate the local crystal field and potentially influence the coordination symmetry and photoluminescence behavior of the host lattice. Since Tb^{3+} and Gd^{3+} are isovalent, no charge imbalance is expected upon substitution; thus, the role of K^+ and Li^+ is attributed to lattice distortion and local environment modification rather than charge compensation.

This study systematically investigates the intrinsic photoluminescence behavior of Tb^{3+}-only doped NGBO phosphors and explores the influence of alkali ion co-doping (K^+, Li^+) on emission efficiency and color coordinates under n-UV excitation. Unlike previous studies that relied on sensitizer-mediated energy transfer, this work demonstrates the efficient direct excitation of Tb^{3+} ions in NGBO, eliminating the need for sensitizer ions such as Ce^{3+}. This simplified design not only enhances structural stability and spectroscopic clarity, but also first-time application of Judd–Ofelt analysis in this host, providing a new framework for evaluating local symmetry and photonic performance in Tb^{3+}-based phosphors. The phosphors were synthesized via a conventional high-temperature solid-state reaction. Structural properties were characterized by XRD and refined using the Rietveld method. Local vibrational modes were probed via Raman and FTIR spectroscopy. Photoluminescence characteristics, including excitation and emission spectra, decay kinetics, and CIE chromaticity coordinates, were evaluated under both room and cryogenic temperatures. To the best of our knowledge, no prior J-O analysis has been reported for Tb^{3+}-doped NGBO phosphors. This study presents the first systematic application of J-O theory to this specific host lattice, providing new insights into the local coordination environment of Tb^{3+} ions. While J-O analyses have been previously applied to rare-earth-doped systems such as Eu^{3+} in $Ca_3Nb_2O_8$ [9], Tb^{3+} in $LaAlO_3$ [10], and more recently, Tb^{3+} in the borate-based $K_7SrY_2(B_5O_{10})_3$ [11], such analysis has not yet been conducted for Tb^{3+} in NGBO. By extracting intensity parameters (Ω_2, Ω_4, Ω_6) from emission spectra and evaluating radiative probabilities, branching ratios, and lifetimes, this work contributes original quantitative insights into how alkali ion co-doping modifies the local symmetry and electronic transition dynamics of Tb^{3+} ions in borate hosts.

Experiments

Experimental procedure

Nanostructured NGBO phosphors were synthesized via a microwave-assisted gel combustion method. This technique offers rapid synthesis and enhanced phase purity suitable for optical applications. Analytical grade sodium nitrate ($NaNO_3$), gadolinium oxide (Gd_2O_3), and boric acid (H_3BO_3) (Sigma-Aldrich, ≥99.0 %) were employed as oxidizing precursors. Gd_2O_3 was initially dissolved in 0.1 N HNO_3 under gentle heating to ensure complete solubilization, enhancing precursor compatibility in the aqueous medium. Boric acid and $NaNO_3$ were subsequently added, followed by the introduction of ultrapure water (18.2 MΩ·cm) to adjust the total volume to 25 mL.

Citric acid, used as a complexing fuel due to its chelating ability and controlled combustion behavior, was added in a stoichiometric ratio according to the total oxidizing and reducing valences, maintaining an oxidizer-to-fuel (O/F) ratio close to unity to ensure a self-sustaining and clean combustion reaction. For dopant incorporation, terbium (IV) oxide (Tb_4O_7, 99.99 %, Sigma-Aldrich) was introduced at varying weight concentrations (0.5, 1, 2, 3, 5, and 7 wt%) relative to the total cation content. Additionally, co-doping strategies were explored using lithium nitrate ($LiNO_3$, Merck, 99.9 %) and potassium nitrate (KNO_3, Merck, 99.9 %) to study the influence of Li^+ and K^+ on lattice structure and photoluminescence behavior. These dopants were incorporated at the same concentration levels as Tb^{3+} to enable comparative analysis. In the NGBO lattice, Tb^{3+} ions are expected to substitute for Gd^{3+} ions due to their comparable trivalent charge and ionic radii. Similarly, Li^+ and K^+ ions were intended to partially replace Na^+ sites, owing to their monovalent nature and similar ionic sizes, while preserving charge neutrality in the structure.The precursor solution was magnetically stirred at 80 °C for 1 h under reflux using a watch glass cover to promote uniform gelation. Upon attaining a viscous gel consistency, the mixture was transferred to a ceramic crucible and subjected to microwave irradiation in a 2.45 GHz domestic microwave oven (800 W). Within seconds, the sample exhibited rapid foaming and ignition, resulting in a self-propagating combustion reaction. The exothermic process produced voluminous, fluffy powders indicative of rapid gas evolution and crystallite formation. The obtained powders were subsequently calcined at 900 °C for 4 h in a muffle furnace to enhance crystallinity and eliminate residual organic matter. Controlled natural cooling to room temperature over 24 h was employed to prevent thermal stress. The resulting NGBO nanopowders were stored in a vacuum desiccator to prevent atmospheric moisture absorption prior to characterization.

Characterization techniques

The phase composition and crystalline structure of the synthesized NGBO:Tb^{3+},Li^+/Na^+ phosphors were examined by XRD using a Malvern Panalytical Empyrean diffractometerequipped with Cu-Kα radiation (λ = 1.5418 Å), operated at 40 kV and 45 mA. XRD patterns were collected in the 2θ range of 10°–80° at ambient conditions. The obtained patterns were subjected to Rietveld refinement using appropriate

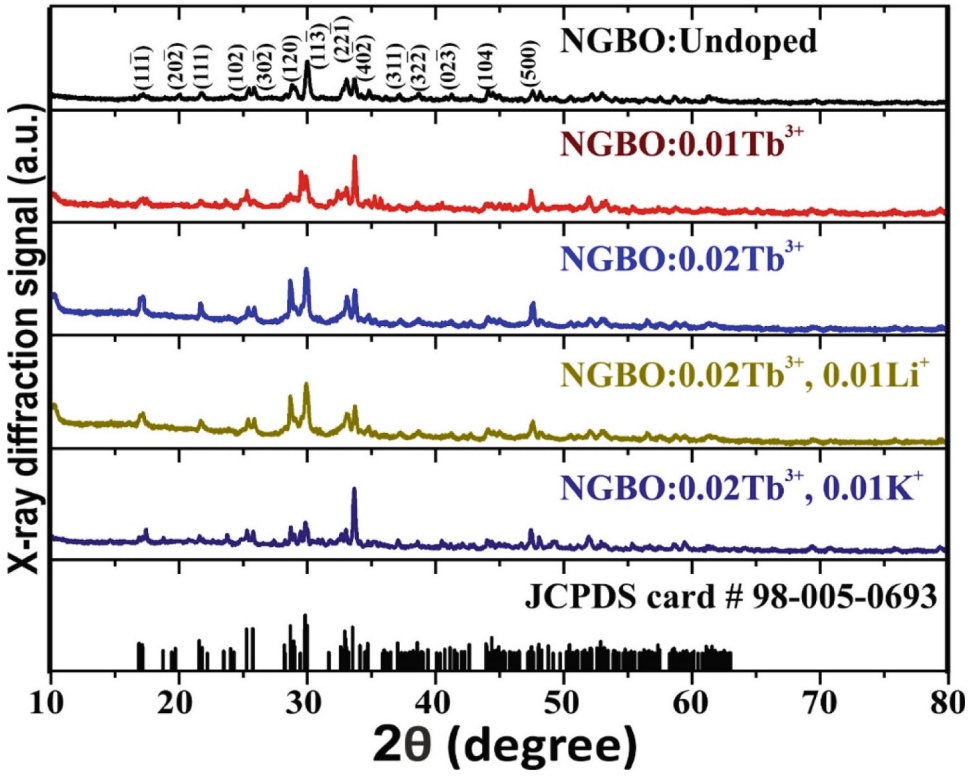

(a)

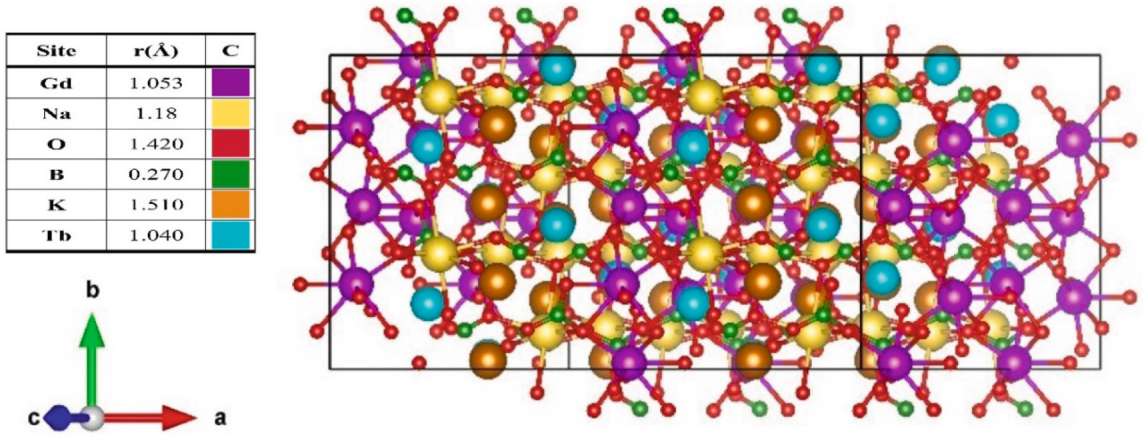

(b)

Fig. 1. (a) Powder XRD patterns of undoped, Tb^{3+}-doped, and alkali co-doped NGBO samples, showing single-phase monoclinic structure indexed to JCPDS #98–005-0693. (b) Crystallographic model of the $Na_2Gd_2B_2O_7$:Tb^{3+},K^+ system, visualized using VESTA. Gd^{3+}/Tb^{3+} ions occupy distorted LnO_8 sites, while K^+ and Na^+ are located in irregular polyhedral voids. (c) Rietveld refinement profiles of undoped, Tb^{3+}-doped (1 and 2 wt%), and alkali co-doped (2 wt% Tb^{3+} with 1 wt% Li^+ or K^+) NGBO samples. (d) Williamson–Hall plots (UDM model) for undoped, Tb^{3+}-doped, and alkali co-doped NGBO samples.

crystallographic software (Highscore-plus) to determine phase purity, unit cell parameters, and average crystallite size.

Surface morphology and microstructural features were investigated using a Zeiss scanning electron microscope (SEM) coupled with an energy-dispersive X-ray spectroscopy (EDS) system for compositional analysis. Prior to imaging, powder samples were sputter-coated with a thin gold (Au) layer to enhance surface conductivity and minimize charging effects during SEM operation.

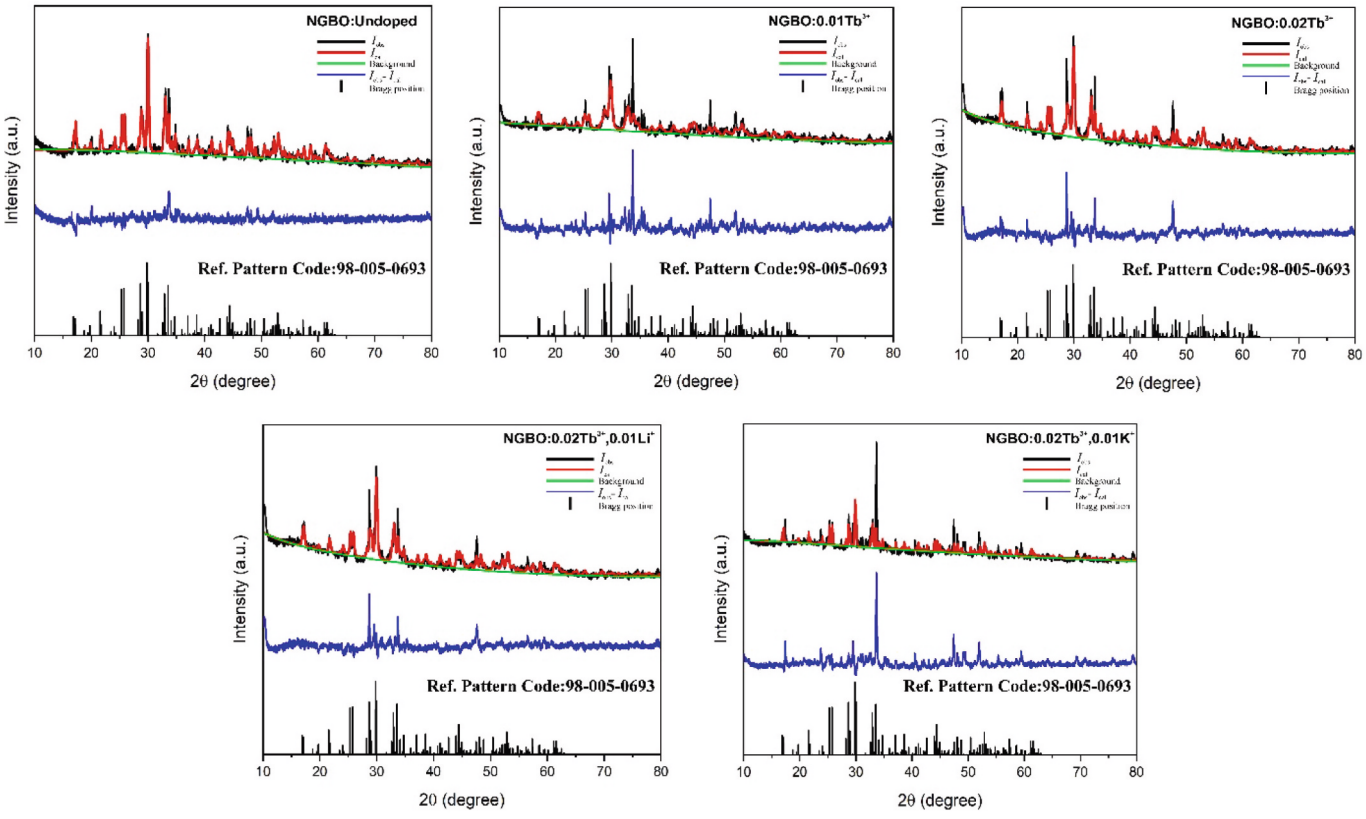

(c)

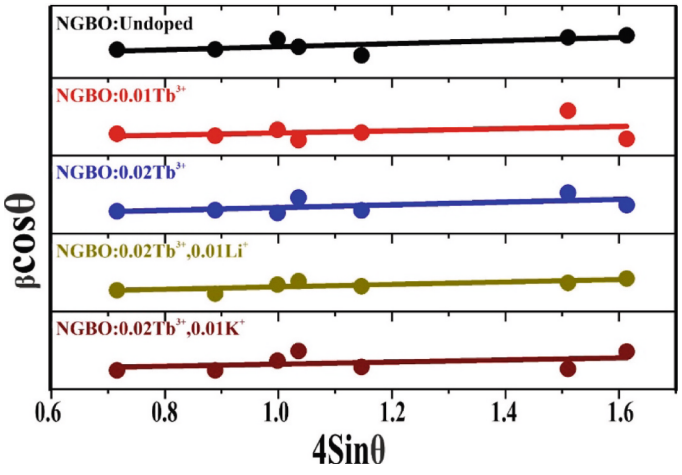

(d)

Fig. 1. (*continued*).

To assess chemical bonding and functional group distribution within the host lattice, FTIR spectroscopy was carried out using a Thermo Scientific Nicolet iS50 spectrometer over the spectral range of 4000–400 cm^{-1}. Complementary vibrational analysis was performed via Raman spectroscopy using a Renishaw inVia Raman microscope with a 532 nm excitation laser and 2400 lines/mm diffraction grating, providing insights into lattice dynamics and phonon modes.

Photoluminescence (PL) and photoluminescence excitation (PLE) spectra were measured with an Edinburgh Instruments FS5 spectrofluorometer utilizing a xenon lamp as the excitation source. Spectroscopic measurements were conducted at room temperature and extended up to 500 K to investigate thermal quenching behaviour. The thermal stability and activation energy of luminescence processes were evaluated by analysing the temperature-dependent emission intensity and spectral shifts.

Results and discussion

XRD and Rietveld analysis

To assess the structural integrity and phase evolution of Tb^{3+}-doped and alkali-modified NGBO phosphors, XRD was conducted on undoped

Table 1
Refined lattice parameters of undoped, Tb^{3+}-doped (1 and 2 wt%), and alkali ion co-doped NGBO samples obtained from Rietveld refinement of XRD data.

Unit Cell	NGBO Undoped	0.01 Tb^{3+}	0.02 Tb^{3+}	0.02 Tb^{3+},0.01Li^{+}	0.02 Tb^{3+},0.01 K^{+}
a [Å]	10.69875	10.60157	10.65932	10.65821	10.68572
b [Å]	6.32438	6.33921	6.31963	6.32306	6.32017
c [Å]	10.33109	10.32185	10.33998	10.33508	10.32606
beta [°]	117.8148	117.5684	117.8708	117.8517	117.781
Vol. [$Å^3$]	618.2665	614.9242	615.7362	615.8229	616.9932
χ^2	1.956	3.511	3.394	2.948	4.403
R_p	0.032	0.035	0.032	0.029	0.043
R_{wp}	0.043	0.052	0.050	0.043	0.067
R_{exp}	0.022	0.015	0.014	0.014	0.015

NGBO, NGBO:Tb^{3+} (1 and 2 wt%), and co-doped variants incorporating Li^{+} and K^{+} (1 wt% each). As shown in Fig. 1a, all diffraction patterns are in agreement with the standard JCPDS card #98–005-0693, confirming that the monoclinic crystal structure (space group $P2_1/c$) is preserved across all compositions. The absence of impurity peaks indicates successful incorporation of both the activator (Tb^{3+}) and the alkali co-dopants into the host lattice, without inducing secondary phases. The corresponding crystallographic model, visualized in Fig. 1b using VESTA software, reveals that Gd^{3+}/Tb^{3+} ions are situated in distorted LnO_8 dodecahedra. Meanwhile, K^{+} and Na^{+} ions occupy irregular polyhedral sites, emphasizing the structural complexity and compositional flexibility of the NGBO framework.

To further explore dopant behavior, the crystal structure was modeled to assess site preference and potential lattice perturbations. Given the close match in ionic radii between Gd^{3+} (0.938 Å) and Tb^{3+} (0.923 Å) in eightfold coordination, Tb^{3+} is expected to substitute for Gd^{3+} with minimal distortion. This hypothesis is supported by Rietveld refinement results, which show only slight variations in unit cell parameters and monoclinic distortion metrics upon Tb^{3+} doping.

In parallel, K^{+} ions were modelled at Na^{+} lattice positions based on charge neutrality and site accessibility within the NGBO framework. Considering the larger ionic radius of K^{+} (1.51 Å) relative to Na^{+} (1.18 Å), local lattice expansion is anticipated and was indeed observed experimentally. Structural visualization using VESTA software confirms that K^{+} ions adopt irregular polyhedral coordination environments, while the lanthanide ions (Gd^{3+}/Tb^{3+}) retain coordination within distorted LnO_8 dodecahedra.

Overall, the NGBO host lattice demonstrates excellent structural tolerance to dual doping. Both experimental diffraction patterns and theoretical modelling affirm that the long-range monoclinic order is preserved, highlighting the suitability of this borate framework for further rare-earth doping and photonic device integration.

To further evaluate the impact of dopant concentration and alkali ion incorporation on crystallographic parameters, Rietveld refinement was performed using the FullProf suite (Fig. 1c). It should be noted that the residuals in the Rietveld refinement profiles ($\chi^2 = 2.9–4.4$, $R_{wp} < 7$ %) are well within acceptable limits, and the discrepancy observed in the difference plots, particularly for low-intensity peaks, arises from expected anisotropic strain and preferred orientation effects. These are inherent to the alkali-doped borate systems and do not compromise the validity of the structural model, as supported by phase purity in FTIR, Raman, and EDS analyses. The refinement residuals (χ^2, R_p, R_{wp}, and R_{exp}) remained within acceptable limits, affirming the goodness-of-fit.

Table 1 summarizes the refined lattice parameters. Compared to the undoped host ($a = 10.6987$ Å, $\beta = 117.81°$), the introduction of 1–2 wt% Tb^{3+} results in a subtle contraction of the a and c axes, consistent with the slightly smaller ionic radius of Tb^{3+} (0.923 Å for CN = 8) relative to Gd^{3+} (0.938 Å).

Interestingly, co-doping with monovalent alkali ions induces distinguishable yet systematic lattice distortions. For example, the a-axis parameter in NGBO:0.02 Tb^{3+},0.01 K^{+} expands to 10.6857 Å, while the Li^{+}–co-doped counterpart exhibits a slightly contracted unit cell. Notably, in the XRD pattern of NGBO:0.02 Tb^{3+},0.01 K^{+}, enhanced peak intensities for specific planes suggest the development of preferential orientation. This is likely due to the anisotropic strain relaxation and localized distortion introduced by K^{+} substitution, which may favor oriented crystal growth during high-temperature calcination. These modifications are attributable to the differing ionic sizes and field strengths of K^{+} (1.51 Å) and Li^{+} (0.92 Å), which perturb the local coordination environments and lattice strain in opposing manners. The observed changes in unit cell volume ($\Delta V \approx \pm 1.2$ $Å^3$) reinforce the conclusion that alkali ions are effectively incorporated and contribute to subtle lattice distortion without inducing structural instability.

These findings are in strong agreement with prior studies by Sakthivel et al. [8], who conducted similar refinements on Eu^{3+}-activated NGBO phosphors. Their report likewise confirmed the stability of the monoclinic phase upon rare-earth substitution and demonstrated minimal perturbation of the host lattice. Our results extend this structural understanding to the Tb^{3+}-only doping regime and further reveal that alkali ion co-doping can serve as an effective strategy for tailoring local symmetry and electronic environments—an essential prerequisite for modulating photoluminescent behavior.

In order to gain deeper insight into the microstructural characteristics of Tb^{3+}-doped and alkali-ion-modified NGBO phosphors, crystallite size (D), lattice strain (ε), and dislocation density (δ) were estimated using both the Scherrer equation and the Williamson–Hall (W–H) method. These analyses, derived from peak broadening in the X-ray diffraction patterns, provide essential information on the influence of dopant-induced lattice perturbations at the nanoscale level.

The Scherrer equation [12] was applied to the most intense diffraction peaks to estimate crystallite sizes:

$$D = \frac{K\lambda}{\beta cos\theta} \quad (1)$$

where K is the shape factor (assumed to be 0.9), λ is the X-ray

Table 2
Crystallite size (D), dislocation density (δ), and microstrain (ε) values of undoped, Tb^{3+}-doped, and alkali co-doped NGBO samples as estimated from Scherrer and Williamson–Hall (UDM) analyses.

Concentration		Undoped	0.01 Tb^{3+}	0.02 Tb^{3+}	0.02 Tb^{3+},0.01Li^{+}	0.02 Tb^{3+},0.01 K^{+}
Scherrer	D (nm)	57	62	64	61	52
	$\delta \times 10^{-3}$ (nm^{-2})	0.3066	0.2576	0.2440	0.2645	0.3737
Williamson-Hall	D (nm)	61	68	71	65	53
	$\varepsilon \times 10^{-2}$	2.32	1.93	2.31	1.63	1.05

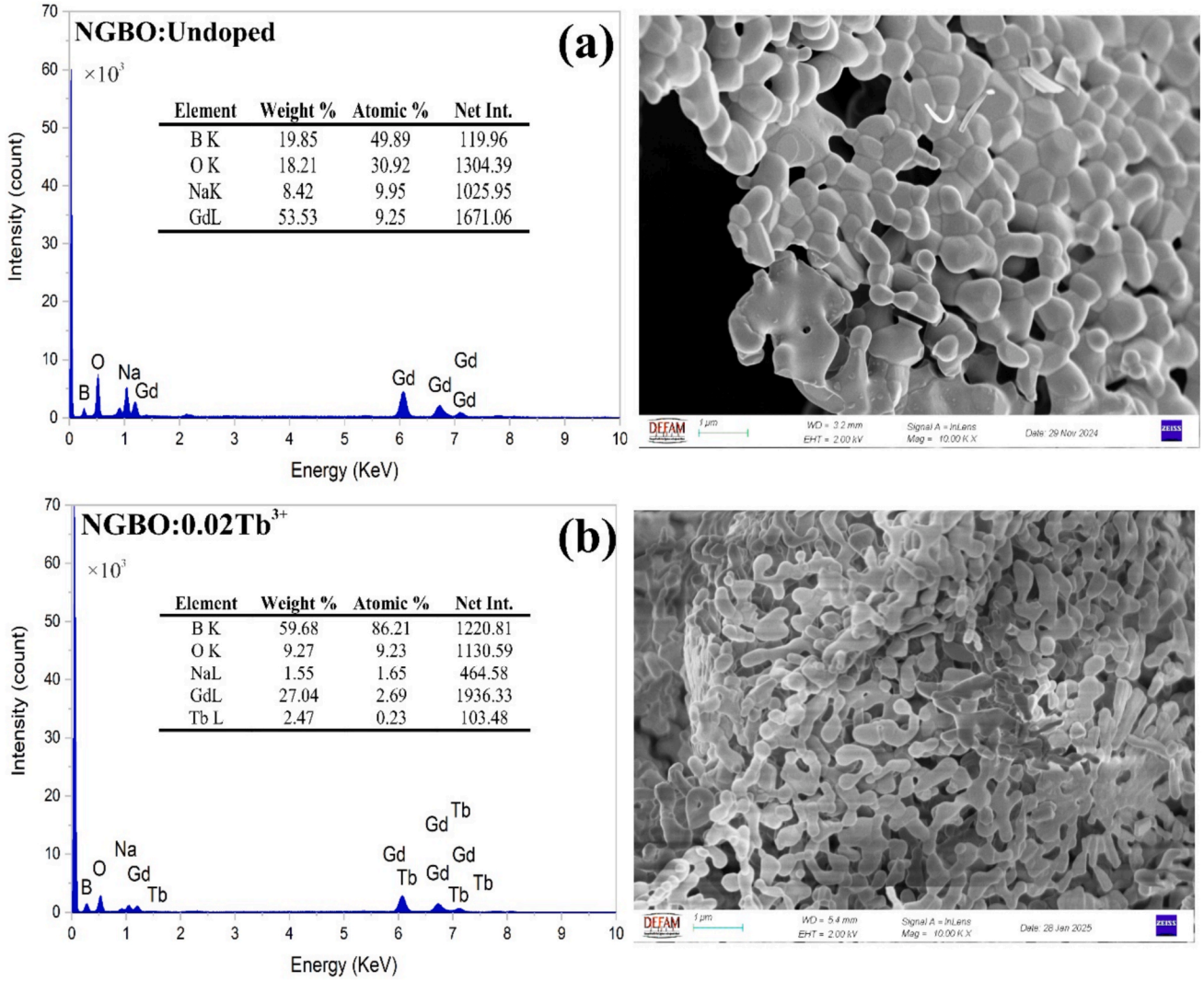

Fig. 2. SEM micrographs and EDS spectra of (a) undoped and (b) Tb^{3+}-doped (2 wt%) NGBO samples. The morphology evolves from smooth, compact grains to more textured and porous structures upon doping. EDS results confirm successful Tb incorporation and maintain the elemental stoichiometry of the host lattice.

wavelength (Cu-Kα, 1.5406 Å), β is the full width at half maximum (FWHM) in radians, and θ is the Bragg angle. As shown in Table 2, the crystallite sizes estimated by the Scherrer method range from 52 nm (NGBO:0.02 Tb^{3+},0.01 K^{+}) to 64 nm (NGBO:0.02 Tb^{3+}), indicating a slight size reduction in particle size due to lattice strain introduced by larger ionic radius of K^{+}.

To separate the contributions of crystallite size and strain, the Williamson–Hall method was applied using the uniform deformation model (UDM) [13]:

$$\beta cos\theta = \frac{K\lambda}{D} + 4\epsilon sin\theta \quad (2)$$

Fig. 1d shows the linear plots of βcosθ versus 4sinθ, from which the slope and intercept were used to determine microstrain (ε) and crystalline size (D) respectively. The crystallite sizes obtained from W–H analysis (ranging from 53 to 71 nm) are generally larger than those estimated by the Scherrer method, as expected due to the explicit incorporation of strain. Notably, the undoped and 0.02 Tb^{3+} samples exhibit the largest crystallite sizes (~68–71 nm), while the 0.02 Tb^{3+},0.01 K^{+} composition yields the smallest crystallites (53 nm), suggesting increased lattice disorder due to K^{+} substitution.

In terms of lattice strain, the undoped NGBO exhibits the highest microstrain (2.32×10^{3}), which slightly decreases upon Tb^{3+} doping ($1.93–2.31 \times 10^{3}$) and is most effectively suppressed by K^{+} co-doping (1.05×10^{3}). This strain relaxation effect is likely due to partial lattice reorganization or compensatory interaction between K^{+} ions and surrounding oxygen framework. The dislocation density (δ), estimated using $\delta = 1/D^{2}$, showed a trend consistent with grain refinement, further confirming the structural impact of alkali doping. A detailed summary of the extracted crystallite sizes, microstrains, and dislocation densities is presented in Table 2. These quantitative results complement the W–H linear plots and collectively confirm that alkali ion co-doping, particularly with K^{+}, leads to reduced crystallite sizes and suppressed internal strain.

These results demonstrate that alkali ion co-doping, particularly with K^{+}, not only influences unit cell parameters but also plays a significant role in modulating microstrain and crystallite coherency—factors that are intimately linked to defect states and, consequently, the luminescence behavior of the phosphor.

Morphological and compositional analysis (SEM–EDS)

The surface morphology and elemental composition of undoped and Tb^{3+}-doped NGBOphosphors were examined using SEM combined with EDS. Fig. 2a depicts the microstructure of the undoped NGBO sample, comprising irregularly shaped, aggregated grain clusters with relatively

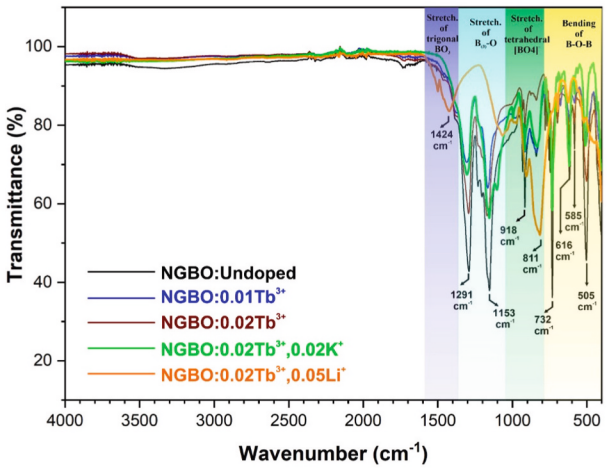

(a)

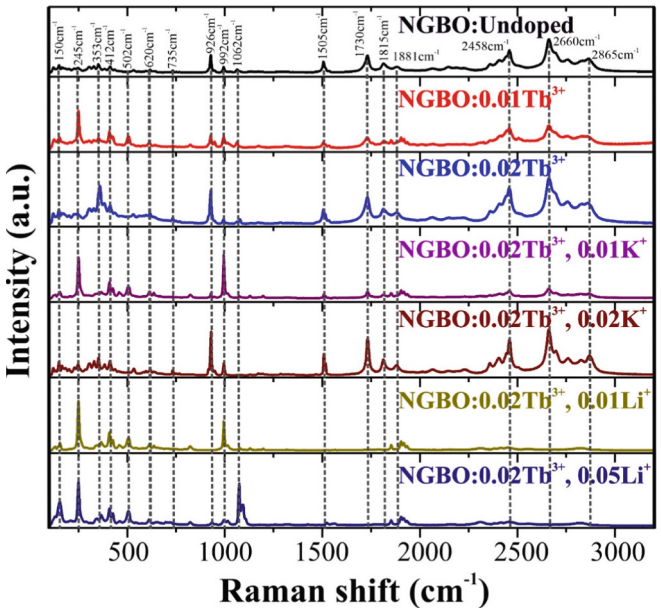

(b)

Fig. 3. (a)FTIR spectra of undoped, Tb^{3+}-doped, and alkali ion co-doped NGBOsamples recorded at room temperature. The labeled bands correspond to characteristic stretching and bending modes of BO_3 and BO_4 units. Minor peak shifts upon doping suggest local structural perturbations without disrupting the borate lattice. (b) Raman spectra of undoped and Tb^{3+}/alkali co-doped NGBO samples recorded at room temperature. The vibrational modes correspond to characteristic BO_3 and BO_4 units.

smooth surfaces. The grains are densely packed, forming a continuous network with minimal porosity, indicating efficient solid-state diffusion during synthesis.

With the incorporation of 2 wt% Tb^{3+} (Fig. 2b), a noticeable morphological change is observed. The particle agglomerates appear more fragmented, exhibiting increased surface texture and pore-like intergranular features. This microstructural change may result from minor disruptions in grain growth dynamics caused by Tb^{3+} substitution at Gd^{3+} sites, which may affect local diffusion barriers or promote heterogeneous nucleation during sintering.

The EDS spectra confirm the presence of all expected constituent elements—Na, Gd, B, and O—in both undoped and Tb^{3+}-doped samples. In the undoped NGBO sample, the quantitative analysis reveals approximate atomic ratios consistent with the stoichiometric formula of $Na_2Gd_2B_2O_7$. Notably, the EDS spectrum of the Tb^{3+}-doped sample shows distinct peaks for Tb (at ~ 7.5 keV and ~ 1.2 keV for L and M lines, respectively, confirming the successful incorporation of Tb ions into the host lattice. The measured atomic percentage of Tb^{3+} is approximately 0.23 %, aligning well with the nominal doping level.

Additionally, a slight reduction in Gd content is observed in the doped sample, suggesting that Tb^{3+} ions have substituted for Gd^{3+} sites, which is consistent with their similar ionic radii and charge states. The observed compositional homogeneity, absence of secondary phases or impurities, and the close agreement between nominal and detected concentrations confirm the effectiveness of the solid-state reaction in producing phase-pure, doped NGBO phosphors.

Vibrational analysis: FTIR and Raman spectroscopy

FTIR spectroscopy was used to investigate the vibrational modes associated with the borate network in undoped and doped NGBO phosphors. The FTIR spectra recorded in the range of 400–4000 cm^{-1} are presented in Fig. 3a. A series of well-defined absorption bands between 400 and 1500 cm^{-1} was observed, corresponding to the intrinsic vibrational modes of BO_3 and BO_4 units, which constitute the fundamental structural building blocks of the NGBO lattice.

The broad band at ~ 1424 cm^{-1} is assigned to the asymmetric stretching vibrations of trigonal BO_3 groups, while the shoulder at ~ 1291 cm^{-1} is associated with the B–O stretching of distorted BO_3 units. The prominent peak at ~ 1153 cm^{-1} and its adjacent feature at ~ 918 cm^{-1} are assigned to the asymmetric stretching vibrations of B_3O_6 rings and BO_4 tetrahedra, respectively. The peak near 811 cm^{-1} corresponds to the symmetric stretching of isolated BO_4- units.

Lower-wavenumber bands in the 500–700 cm^{-1} range, including those at ~ 732 cm^{-1}, ~616 cm^{-1}, ~585 cm^{-1}, and ~ 505 cm^{-1}, are attributed to bending modes involving B–O–B linkages and complex borate ring deformations. These features confirm the simultaneous presence of trigonal and tetrahedral borate units within the NGBO host matrix, in agreement with previous studies on rare-earth borate systems [14,15].

Doping with Tb^{3+} and subsequent co-doping with K^+ and Li^+ ions cause subtle shifts in band positions and intensities, particularly in the high-frequency region (1150–1450 cm^{-1}). These spectral variations suggest minor changes in the local bonding environment and distortion of BO_x polyhedral, likely due to lattice strain or symmetry alteration around the dopant sites. No impurity bands were detected in the spectra, indicating that the borate framework remains intact across all compositions.

Notably, no distinct absorption bands were observed in the 3000–3700 cm^{-1} range of the FTIR spectra, which is typically associated with O–H stretching modes arising from hydroxyl groups or adsorbed moisture. The absence of these features suggests a low hydroxyl content within the synthesized phosphors. This is particularly significant for photoluminescent materials, as hydroxyl groups are well-known quenching centers that facilitate non-radiative decay via multiphonon relaxation processes. Kuhn et al. [16] systematically demonstrated that an increased hydroxyl concentration in rare-earth-doped glasses leads to a significant reduction in emission intensity and lifetime due to enhanced non-radiative losses.

Raman spectroscopy was performed to further explore the short-range structural features and bonding environments in undoped and Tb^{3+}/alkali co-doped NGBO samples. The Raman spectra in the 200–3000 cm^{-1} range are presented in Fig. 3b. All samples display sharp, well-resolved peaks, highlighting the crystalline characteristics of the NGBO matrix.

The dominant bands below 1000 cm^{-1} are primarily associated with symmetric and asymmetric stretching vibrations of borate structural units. Specifically, the peaks near 420 cm^{-1}, 585 cm^{-1}, and 732 cm^{-1} correspond to bending and deformation modes of B–O–B linkages within BO_3 triangles and BO_4 tetrahedra. The bands at ~ 918 cm^{-1} and 1153

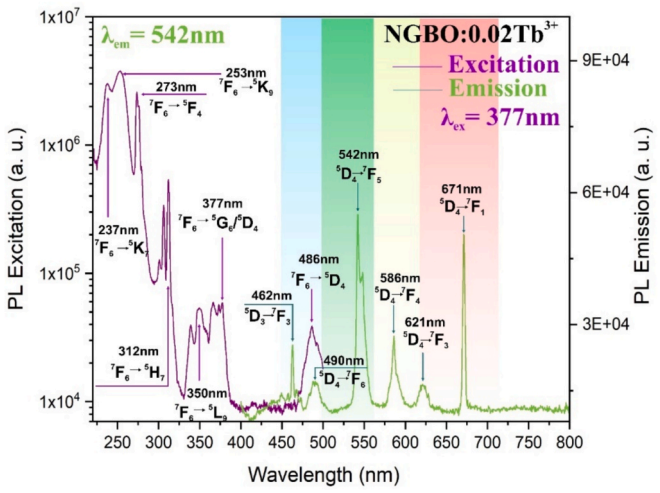

Fig. 4. Photoluminescence excitation and emission spectra of 2 wt% Tb^{3+}-doped NGBO phosphors measured at room temperature.

cm^{-1} are assigned to the asymmetric stretching modes of BO_4 units and B_3O_6 ring structures, consistent with the assignments observed in the FTIR spectra and previously reported Raman spectral studies of alkali borate glasses [17].

A high-frequency band around 1424 cm^{-1}, also observed in FTIR, is visible in the Raman spectra and corresponds to the stretching vibration of trigonal BO_3 groups. Notably, the Li^+ and K^+ co-doped samples exhibit slight shifts in peak positions and relative intensities, particularly around 810–920 cm^{-1}, indicating subtle changes in borate network connectivity and BO_4/BO_3 unit ratios. These modifications are likely induced by local lattice distortion and field-induced polarization effects caused by alkali ions.

Furthermore, the appearance of weak bands at ~ 2458 cm^{-1} and ~ 2660 cm^{-1} in certain compositions may be attributed to overtone or combination modes, which are commonly observed in ordered borate networks. The overall spectral features indicate the retention of the borate framework, along with the coexistence of trigonal and tetrahedral boron coordination geometries. These findings support the presence of mixed BO_3 and BO_4 units and their structural evolution as a function of dopant concentration, in agreement with earlier Raman-based studies on lithium borate glass systems [18]. Although the FTIR and Raman spectra do not reveal fundamentally new vibrational modes, their inclusion in this study is essential for validating the structural integrity of the host matrix. The confirmed coexistence of BO_3 and BO_4 units, together with the absence of hydroxyl-related absorption bands, directly supports the observed high photoluminescence efficiency by indicating low non-radiative defect density. Additionally, the subtle shifts in peak positions upon Tb^{3+} and alkali ion incorporation reflect dopant-induced lattice distortion and symmetry modulation. These vibrational features complement the XRD, PL, and lifetime data, establishing a coherent picture of a stable, defect-controlled, and optically favorable environment. Therefore, these spectra are not only methodologically relevant but substantiate the structural robustness and functional potential of the NGBO phosphors.

Photoluminescence properties of Tb^{3+}-Doped NGBO phosphors

Fig. 4 presents the PL excitation and emission spectra of the 2 wt% Tb^{3+}-doped NGBO phosphors measured at room temperature. The excitation spectrum, monitored at the $^5D_4 \rightarrow {}^7F_5$ emission peak (λ_{em} = 542 nm), displays a series of sharp lines attributed to f–f transitions within the Tb^{3+} $4f^8$ electronic configuration. Notable excitation peaks include transitions at 237 nm ($^7F_6 \rightarrow {}^5K_8$), 253 nm ($^7F_6 \rightarrow {}^5K_9$), 273 nm ($^7F_6 \rightarrow {}^5F_4$), 312 nm ($^7F_6 \rightarrow {}^5H_6$), 350 nm ($^7F_6 \rightarrow {}^5L_1^0$), and a prominent band at 377 nm ($^7F_6 \rightarrow {}^5G_6/{}^5D_3$). Among these, the 377 nm transition exhibits the highest intensity, indicating its suitability as the optimal excitation wavelength for green luminescence.

Under 377 nm excitation, the emission spectrum exhibits multiple well-resolved peaks corresponding to the $^5D_4 \rightarrow {}^7F_j$ (J = 6, 5, 4, 3, 2, 1) transitions of Tb^{3+}. The strongest peak is observed at 542 nm ($^5D_4 \rightarrow {}^7F_5$), producing intense green luminescence. Additional emission bands appear at 490 nm ($^5D_4 \rightarrow {}^7F_6$), 586 nm ($^5D_4 \rightarrow {}^7F_4$), 621 nm ($^5D_4 \rightarrow {}^7F_3$), and 671 nm ($^5D_4 \rightarrow {}^7F_1$), which are consistent with the magnetic dipole–allowed and parity-forbidden transitions expected in a low-symmetry crystal field environment. The persistent dominance of the green emission band centered around ~ 542 nm across various excitation wavelengths highlights the robustness of the $^5D_4 \rightarrow {}^7F_5$ radiative transition in Tb^{3+} ions. This excitation-independent emission behavior indicates the efficient population of the $^5D_4$ level through multiple excitation channels and suggests that the local crystal field environment around Tb^{3+} remains structurally stable, ensuring consistent spectral output irrespective of the excitation route [19,20].

The spectral features and their intensity distributions indicate efficient 4f–4f radiative transitions within Tb^{3+} ion. The absence of broadband emission from the host lattice, unlike the undoped sample, further confirms that the observed luminescence originates solely from the Tb^{3+} centers. The sharp intensity and resolution of these transitions suggest that Tb^{3+} ions occupy well-defined, low-symmetry sites within the NGBO lattice, which is further supported by similar reports on alkali-modified borate hosts [11].

These findings are consistent with prior studies, where 377 nm excitation has been demonstrated as an efficient resonant pump for populating the $^5D_4$ level via $^5G_6$ and $^5D_3$ intermediate states, followed by non-radiative relaxation and strong green emission from $^5D_4$ [11]. The sharpness and intensity of the PL lines confirm the successful incorporation of Tb^{3+} into optically active sites, reinforcing the potential of NGBO as a promising green-emitting phosphor under near-UV excitation for solid-state lighting applications.

Photoluminescence properties of NGBO:Tb^{3+} with and without alkali ion Co-Doping

The photoluminescence (PL) emission spectra of NGBO:*x* Tb^{3+}, with *x* ranging from 0.5–7 wt%, under 377 nm excitation are presented in Fig. 5a. All samples exhibit well-defined emission bands arising from the characteristic 4f–4f transitions of Tb^{3+} ions. The most intense peak at approximately 541 nm corresponds to the $^5D_4 \rightarrow {}^7F_5$ transition, which is responsible for dominant green emission. Additional transitions, including $^5D_4 \rightarrow {}^7F_6$ (~490 nm), $^5D_4 \rightarrow {}^7F_4$ (~585 nm), and $^5D_4 \rightarrow {}^7F_3$ (~620 nm), are also observed, confirming the typical green emission profile of Tb^{3+} in a low-phonon energy host lattice.

As the Tb^{3+} concentration increases, the PL intensity gradually increases, reaching a maximum at 2 wt% Tb^{3+}, beyond this point, a noticeable decline is observed, as illustrated in Fig. 5b. This behavior is indicative of concentration quenching, a common phenomenon in rare-earth-doped phosphors where excessive dopant ions facilitate non-radiative energy transfer between adjacent luminescent centers.

To elucidate the mechanism underlying this quenching behavior, the critical distance (R_c) between Tb^{3+} ions was calculated based on Blasse's model [21]:

$$R_c = 2\left[\frac{3V}{4\pi x_c N}\right]^{1/3} \quad (3)$$

Here, *V* is the unit cell volume (615.7362 $Å^3$), x_c is the critical concentration at maximum emission intensity (0.02), and *N* is the number of cationic sites per unit cell available for Tb^{3+} substitution. In the case of $Na_2Gd_2B_2O_7$, each formula unit contains two Gd^{3+} ions, and the unit cell contains four formula units ($Z = 4$), resulting in $N = 8$. Substituting these parameters into the classical expression proposed by Blasse, the

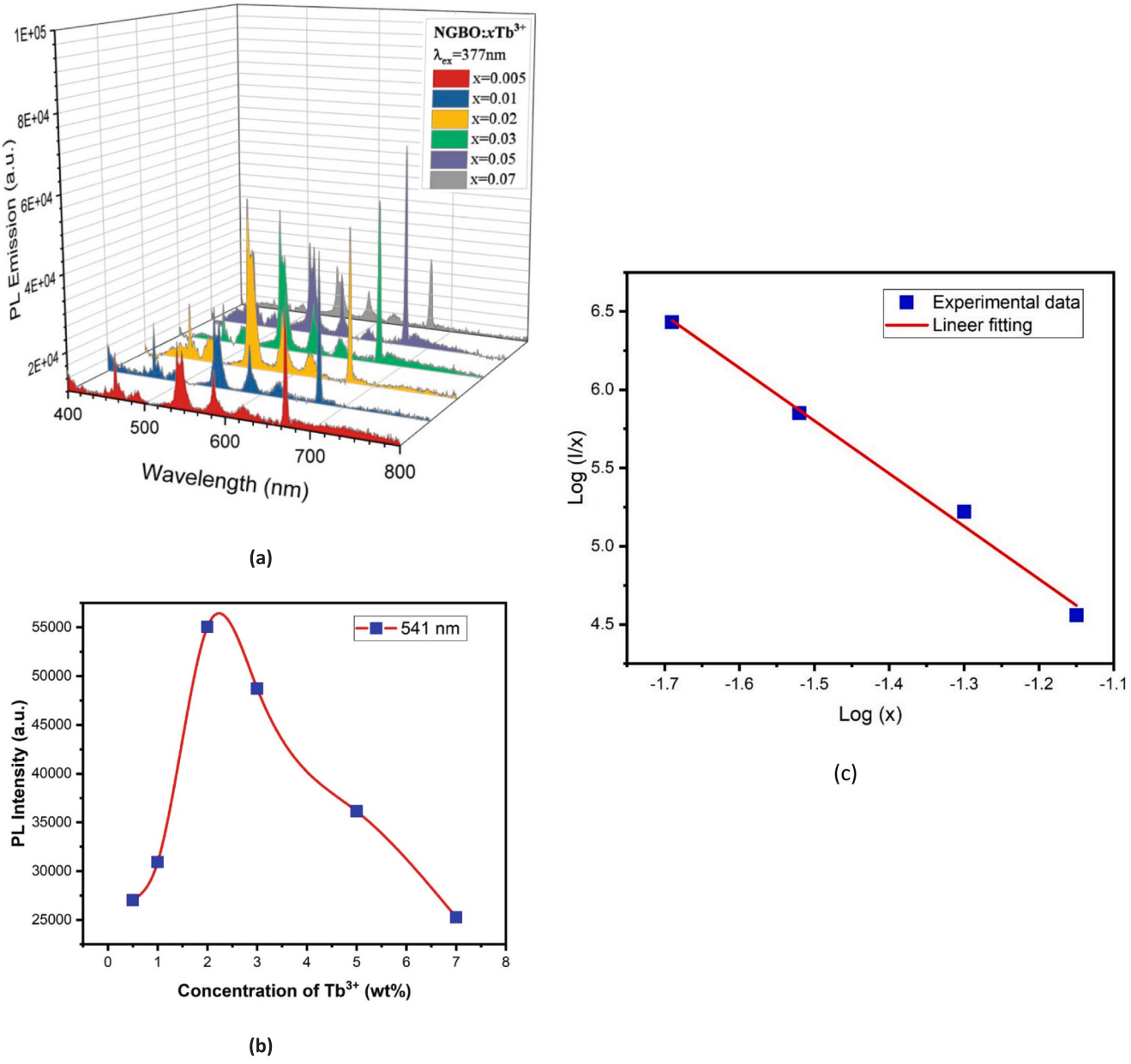

Fig. 5. (a) 3D photoluminescence (PL) emission spectra of NGBO:x Tb^{3+} (x = 0.5–7 wt%) phosphors excited at 377 nm and recorded at room temperature, showing characteristic $^5D_4^7F_J$ transitions. (b) Variation of integrated PL intensity at 541 nm as a function of Tb^{3+} concentration (x), demonstrating optimal emission at$x$ = 2 wt % prior to concentration quenching. (c) Logarithmic plot of $log(I/\chi)$ versus $log(\chi)$ for NGBO:Tb^{3+} samples based on integrated emission intensity at 541 nm, used to evaluate interaction mechanisms causing concentration quenching.

calculated R_c value was determined to be approximately 19.42 Å. The obtained critical distance of 19.42 Å significantly exceeds the 5 Å threshold typically associated with exchange interactions. Consequently, the dominant energy transfer mechanism is not attributed to direct exchange interactions, but rather to multipolar mechanisms—most likely electric dipole–dipole coupling, as explained by Dexter's theory. This result aligns well with previous studies on $Tb3^+$-activated borate systems, where similar concentration quenching behavior was attributed to long-range multipolar interactions [22]. Comparable multipolar energy transfer mechanisms have also been reported in other Tb^{3+}-doped systems, including $Ba_3(ZnB_5O_{10})PO_4$:Tb^{3+} [22] and $Na_2Y_2TeB_2O_{10}$:Tb^{3+} [23], where the calculated R_c values exceed 5 Å. Notably, in the latter system, further analysis using Dexter's equation confirmed that dipole–quadrupole interactions played a significant role in the quenching process at high activator concentrations, thereby supporting our findings for the NGBO host.

Accordingly, 2 wt% Tb^{3+} is identified as the optimal doping concentration for achieving maximum green emission intensity in the NGBO host. At higher concentrations, the increased likelihood of non-radiative cross-relaxation among Tb^{3+} ions results in reduced PL efficiency. The energy transfer among activator ions surpasses radiative recombination, thereby leading to observed quenching effect. This finding underscores the importance of carefully optimizing dopant concentrations to achieve high luminescent performance in rare-earth phosphors. To further elucidate the non-radiative energy transfer mechanism underlying concentration quenching, a detailed multipolar interaction analysis was performed using the Van Uitert model. While the critical distance calculation ($R_c > 5$ Å) suggests the dominance of long-range multipolar interactions [24], it is essential to quantify the specific interaction type—whether it is electric dipole–dipole, dipole–quadrupole, or quadrupole–quadrupole. This can be accomplished by analysing the relationship between the emission intensity (I) and the Tb^{3+} doping

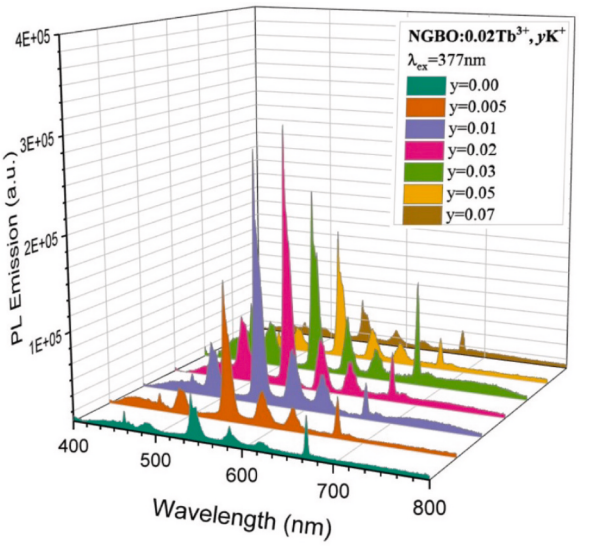

(a)

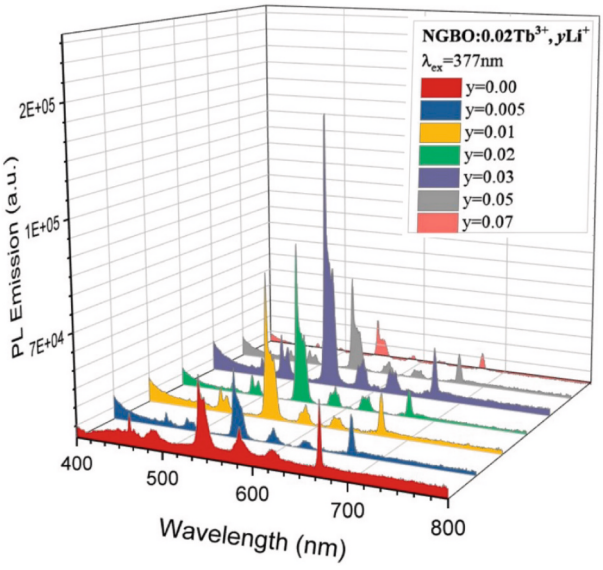

(b)

Fig. 6. PL emission spectra of NGBO:0.02 Tb^{3+} phosphors co-doped with various concentrations of (a) K^+ (y = 0.00–0.07) and (b) Li^+ (y = 0.00–0.07) under 377 nm excitation. The measurements were conducted at room temperature using a 3D configuration to clearly distinguish spectral intensities across different doping levels. All samples exhibit characteristic $^5D_4 \rightarrow {}^7F_j$ transitions of Tb^{3+} ions, with maximum emission intensity near 542 nm, corresponding to the $^5D_4 \rightarrow {}^7F_5$ transition.

concentration (χ), as described by the theoretical model below.

According to the Van Uitert model, the relationship between the luminescence intensity (I) and the activator ion concentration (χ) for multipolar interactions is described by the following expression [25]:

$$log(I/\chi) = A - (\theta/3)log(\chi) \quad (4)$$

where A is a constant and is an interaction parameter that defines the nature of the multipolar coupling. The slope of the linear fit in a plot of $log(I/\chi)$ versus $log(\chi)$ yields $-\theta/3$, from which θ can be calculated. Theoretical values of θ = 6, 8, and 10 correspond to electric dipole–dipole, dipole–quadrupole, and quadrupole–quadrupole interactions, respectively.

In this study, the logarithmic plot of $log(I/\chi)$ versus $log(\chi)$ was constructed for Tb^{3+}-doped NGBO samples based on the integrated emission intensity at 541 nm. As shown in Fig. 5c, the linear regression yielded a slope of approximately − 3.37, corresponding to a calculated θ value of 10.11, which closely matches the theoretical value of 10. These results indicate that the concentration quenching mechanism in NGBO:Tb^{3+} phosphors is primarily governed by electric quadrupole–quadrupole interactions, consistent with the R_c-based prediction and similar findings in borate host systems such as $LABO_3$:Tb^{3+} [26].

These findings confirm that at higher Tb^{3+} concentrations, non-radiative energy transfer in NGBO predominantly occurs via a quadrupole–quadrupole interaction mechanism, as evidenced by the high θ value (~10.11). Although less frequently observed than dipole–dipole coupling, this mechanism can become significant in host lattices with suitable spatial and symmetry conditions, such as $LaBO_3$ [26].

Interestingly, whereas the green emission band centered at 541 nm ($^5D_4 \rightarrow {}^7F_5$) exhibits conventional concentration quenching—peaking at 2 wt% Tb^{3+}—the red emission around 620 nm ($^5D_4 \rightarrow {}^7F_3$) displays a distinct behaviour. As illustrated in the PL spectra, the intensity of the 620 nm band continues to increase with Tb^{3+}concentration up to 5 wt%, after which it begins to decline. This unusual behavior can be attributed to multiple underlying mechanisms.

First, the $^5D_4 \rightarrow {}^7F_3$ transition is parity-forbidden and relatively weak, being hypersensitive to variations in the local crystal field and site symmetry. At elevated Tb^{3+} concentrations, substitution at Gd^{3+} sites may induce local distortions or result in the occupation of lower-symmetry sites, thereby increasing the probability of such weak transitions. Second, higher dopant concentrations may alter the population dynamics of Tb^{3+} energy levels, leading to partial redistribution of excited electrons toward the lower-lying $^7F_3$ levels. Third, as the dominant $^5D_4 \rightarrow {}^7F_5$ emission is quenched, radiative competition may favor alternative channels like $^5D_4 \rightarrow {}^7F_3$, thereby temporarily enhancing the red emission. Similar phenomena have been reported in other Tb^{3+}-activated phosphor systems, often attributed to multiplet splitting and local symmetry distortions.

Consequently, the enhanced 620 nm emission intensity observed up to 5 wt% Tb^{3+} is likely due to a combination of population redistribution, symmetry-driven transition enhancement, and radiative competition—all becoming more prominent under high dopant concentrations. A similar trend was observed in $Sr_3YNa(PO_4)_3F$:Tb^{3+} phosphors, where the 620 nm emission intensity increased with rising Tb^{3+} concentration, despite the absence of a detailed physical explanation in that study [27]. These observations suggest that analogous spectral redistribution phenomena may also occur in other Tb^{3+}-activated host lattices under high dopant concentrations.

Additionally, the effect of alkali ion co-doping on the photoluminescence behavior of NGBO:0.02 Tb^{3+} was systematically investigated using both K^+ and Li^+ as lattice modifiers. As illustrated in Fig. 6a and 6b, co-doping with K^+ ions significantly enhances the PL intensity of the green emission ($^5D_4 \rightarrow {}^7F_5$ at ~ 541 nm), with a maximum observed at y = 0.02 K^+. At this composition, the PL intensity increased by a factor of 5.33 compared to the undoped NGBO:0.02 Tb^{3+} sample, whereas the Li^+–co-doping yielded a 3.41-fold enhancement at y = 0.03Li^+.

This significant enhancement can be attributed to several synergistic mechanisms:

Crystal Field Modification: Substituting Na^+ (1.18 Å) with larger K^+ (1.51 Å) or smaller Li^+ (0.92 Å) ions induces local lattice distortions, modifying the coordination environment around the Tb^{3+} centers. These distortions may relax the parity-forbidden nature of 4f–4f transitions and enhance radiative transition probabilities by perturbing local site symmetry [28].

Reduction of Non-Radiative Centers: Alkali ion co-doping can passivate intrinsic defect states, especially those acting as quenching centers. Raman and FTIR analyses confirm that K^+ and Li^+

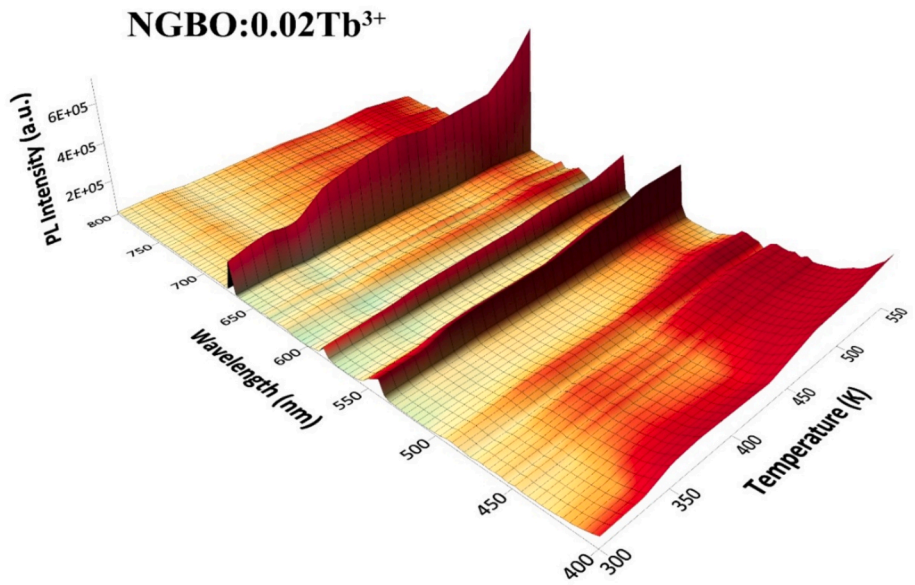

Fig. 7. 3D temperature-dependent PL emission spectra of NGBO:0.02 Tb^{3+} phosphor under 377 nm excitation in the range of 300–500 K, showing a characteristic negative thermal quenching behavior.

incorporation does not disrupt the BO_3/BO_4 framework; instead, it stabilizes the structure, potentially suppressing phonon-assisted non-radiative decay [29].

Enhanced Energy Transfer Efficiency: Alkali-induced lattice distortion may promote greater spatial overlap between donor and acceptor wavefunctions during multipolar interactions. This facilitates stronger radiative channels relative to competing non-radiative losses [30].

Grain Refinement and Strain Relaxation: According to Williamson–Hall and Scherrer analyses (Section 3.1), K^+ co-doping led to a marked reduction in crystallite size and internal lattice strain. The reduced lattice strain may suppress energy dissipation through defect-related pathways, thereby enhancing PL output. Although Li^+ induces slightly less strain relaxation than K^+, it still contributes to microstructural refinement that improves emission efficiency [31].

These findings are consistent with previous studies on alkali co-doping in rare-earth borates, where similar enhancement mechanisms have been proposed to explain improved PL behavior [11,32,33]. Furthermore, the superior enhancement observed with K^+ doping may be attributed to its higher polarizability and greater capacity to disrupt local symmetry compared to Li^+.

Therefore, alkali ion incorporation—particularly that of K^+—is demonstrated to be a highly effective strategy for enhancing the photoluminescent efficiency of NGBO:Tb^{3+} phosphors. The observed enhancement arises not from changes in electronic configuration, but from lattice-mediated effects, including symmetry modulation, defect passivation, and phonon coupling suppression. These results underscore the importance of compositional engineering not only at the activator level, but also within the charge-neutral host framework, offering a versatile pathway to tailor optical performance in high-efficiency solid-state lighting applications.

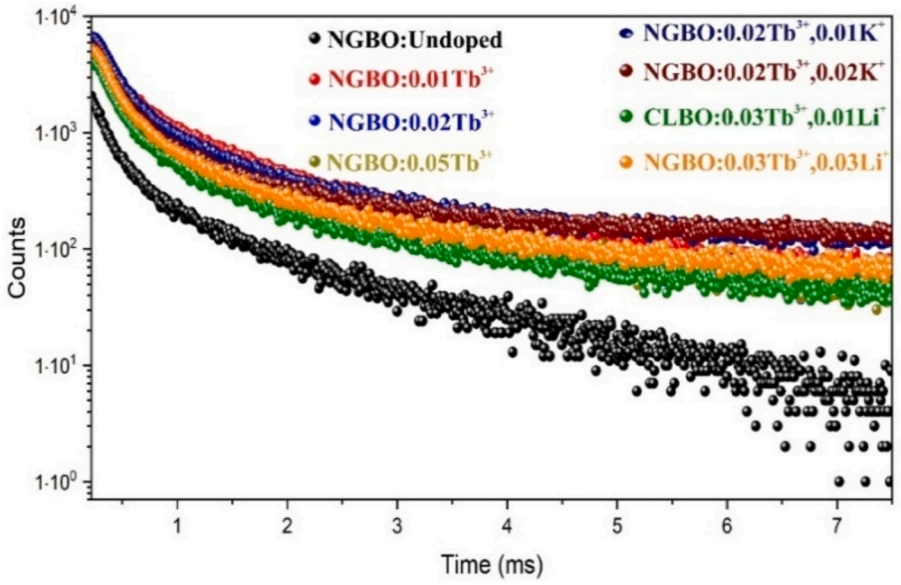

Fig. 8. Time-resolved PL decay curves of NGBO:*x* Tb^{3+} phosphors with and without alkali co-doping, monitored at 541 nm under 377 nm excitation.

Table 3
Fitted lifetime parameters (τ_1, τ_2, τ_3), their relative amplitudes, average lifetime (τ_{avg}), and goodness-of-fit (χ^2) values for NGBO samples with various Tb^{3+} and alkali ion contents.

		Time(μs)	Rel.%	τ_{avg}(ms)	χ^2
NGBO:Undoped	τ_1	13.288 ± 0.105	34.344 ± 0.111	998.586 ± 0.306	1.125 ± 0.028
	τ_2	676.809 ± 0.255	32.317 ± 0.093		
	τ_3	1883.201 ± 0.044	33.339 ± 0.106		
NGBO:0.01 Tb^{3+}	τ_1	16.636 ± 0.105	31.932 ± 0.455	1276.886 ± 0.611	1.211 ± 0.066
	τ_2	621.605 ± 0.222	34.227 ± 0.303		
	τ_3	2028.200 ± 0.069	33.841 ± 0.466		
NGBO: 0.02 Tb^{3+}	τ_1	14.408 ± 0.108	30.748 ± 0.481	1044.236 ± 0.108	1.129 ± 0.023
	τ_2	488.095 ± 0.028	31.106 ± 0.066		
	τ_3	1580.800 ± 0.102	38.146 ± 0.083		
NGBO:0.05 Tb^{3+}	τ_1	14.988 ± 0.507	33.752 ± 0.504	1141.253 ± 0.081	1.281 ± 0.052
	τ_2	546.800 ± 0.662	31.909 ± 0.444		
	τ_3	1804.425 ± 0.206	34.339 ± 0.128		
NGBO:0.02 Tb^{3+},0.01 K^+	τ_1	15.736 ± 0.099	44.429 ± 0.109	1091.961 ± 0.483	1.332 ± 0.073
	τ_2	710.801 ± 0.128	38.404 ± 0.115		
	τ_3	2223.250 ± 0.044	17.167 ± 0.081		
NGBO:0.02 Tb^{3+},0.01Li^+	τ_1	10.032 ± 0.019	35.523 ± 0.305	1271.832 ± 0.482	1.118 ± 0.044
	τ_2	38.444 ± 0.055	33.261 ± 0.199		
	τ_3	1488.815 ± 0.442	31.216 ± 0.144		
NGBO:0.02 Tb^{3+},0.02 K^+	τ_1	16.672 ± 0.336	45.877 ± 0.509	889.469 ± 0.209	1.308 ± 0.039
	τ_2	970.025 ± 0.016	54.123 ± 0.077		
NGBO:0.02 Tb^{3+},0.03Li^+	τ_1	13.028 ± 0.12	30.809 ± 0.426	1093.138 ± 0.071	0.945 ± 0.014
	τ_2	500.401 ± 0.323	35.352 ± 0.299		
	τ_3	1810.842 ± 0.217	33.839 ± 0.410		

Temperature-dependent photoluminescence and evidence of negative thermal quenching

To assess the thermal stability of NGBO:0.02 Tb^{3+} phosphors, temperature-dependent PL measurements were conducted under 377 nm excitation across the 300–550 K range. As shown in Fig. 7, an unusual increase in PL intensity is observed with increasing temperature—opposite to the typical thermal quenching behavior commonly exhibited by rare-earth-doped phosphors. This anomalous behaviour is referred to as negative thermal quenching (NTQ).

In conventional phosphors, elevated temperatures generally activate non-radiative relaxation pathways via multi-phonon processes, thereby reducing emission intensity. However, in the NGBO:Tb^{3+} system, the initial increase in emission intensity with an increasing temperature that thermal energy promotes radiative processes instead of inhibiting them.

This phenomenon is attributed to the thermally activated release of trapped charge carriers initially trapped at intrinsic or alkali-induced shallow energy levels within the host lattice. With increasing temperature, these carriers become thermally liberated and subsequently recombine at the Tb^{3+} luminescent centers, resulting in enhanced radiative emission. Additionally, local distortion induced by alkali co-doping (e.g., K^+ and Li^+) may create a favorable environment for efficient energy transfer under thermal excitation. The observed NTQ behavior in NGBO:Tb^{3+} phosphors is attributed to the thermally stimulated release of charge carriers from shallow trap states, which subsequently recombine radiatively at Tb^{3+} centers. This process competes with conventional non-radiative multi-phonon relaxation mechanisms, and the dominance of radiative recombination over phonon-assisted processes at elevated temperatures leads to the intensity enhancement.

Similar NTQ behavior has also been reported in other borate-based systems, notably in $Na_2Y_2TeB_2O_{10}$:Tb^{3+}, where a comparable intensity increase was attributed to thermally assisted de-trapping from shallow defect levels [23]. These findings confirm that NTQ is not merely an experimental artifact but a genuine, thermally activated process that can be strategically exploited in the design of thermally stable phosphors. The NTQ effect observed in this system is particularly promising for high-power solid-state lighting and optical sensing applications, where conventional thermal quenching typically degrades performance at elevated temperatures [34].

Time-resolved photoluminescence and lifetime analysis

To gain deeper insight into the emission dynamics of Tb^{3+} ions in the NGBO host lattice, time-resolved photoluminescence (TRPL) decay measurements were performed on selected compositions, using 377 nm excitation and monitoring at 541 nm emission corresponding to the $^5D_4 \rightarrow {}^7F_5$ transition. The resulting decay profiles are shown in Fig. 8, with the extracted fitting parameters in Table 3.

All decay curves were satisfactorily fitted using a triple-exponential decay model, expressed as:

$$I(t) = A_1 exp(-t/\tau_1) + A_2 exp(-t/\tau_2) + A_3 exp(-t/\tau_3) \quad (5)$$

where τ_1, τ_2, and τ_3 are decay components, and A_1, A_2, and A_3 are their corresponding amplitudes. The average lifetimes (τ_{avg}) were calculated using the following expression:

$$\tau_{avg} = \frac{A_1\tau_1^2 + A_2\tau_2^2 + A_3\tau_3^2}{A_1\tau_1 + A_2\tau_2 + A_3\tau_3} \quad (6)$$

As presented in Table 3, the undoped NGBO sample exhibits a considerably shorter lifetime (998.586 μs), suggesting the presence of non-radiative recombination centers or surface defects that accelerate carrier relaxation. Upon Tb^{3+}doping, the lifetime increases significantly, with the highest τ_{avg} (1276.886 μs) observed for NGBO:0.01 Tb^{3+}, attributed to optimal spatial separation between activator ions, minimizing cross-relaxation. At the higher Tb^{3+} concentrations (0.02 and 0.05), a moderate decline in lifetime is observed, likely due to increased non-radiative multipolar interactions arising from reduced interionic distances. Furthermore, alkali ion co-doping exerts a notable influence on lifetime dynamics. The NGBO:0.02 Tb^{3+},0.01 K^+ sample exhibits a slightly reduced lifetime (1091.961 μs) compared to its K^+-free counterpart, whereas the Li^+ co-doped sample displays a marginally higher lifetime (1271.832 μs), suggesting that the lighter Li^+ ion may more effectively passivate non-radiative centers or mitigate local strain-induced defects. Notably, the shortest τ_{avg} among the doped samples was observed for NGBO:0.02 Tb^{3+},0.02 K^+ (889.469 μs), potentially due to excessive lattice distortion or concentration quenching. The trends in both decay behavior and lifetime values align with the PL intensity results discussed earlier, further supporting the proposed mechanism of energy transfer and quenching, involving activator clustering and alkali-induced lattice modifications.

Judd–Ofelt analysis of Tb^{3+}-Doped NGBO phosphor

To investigate the radiative properties of the synthesized NGBO:0.02 Tb^{3+} phosphor, a J-O analysis was conducted using the emission spectrum obtained under 377 nm excitation. In this work, the radiative

transition characteristics of Tb^{3+} ions were quantitatively analyzed using the Judd–Ofelt (JO) theory, following the fluorescence decay method described by Luo et al. [35] and Zhang et al. [36]. This approach is particularly suitable for polycrystalline phosphors, where absorption measurements are challenging. In this method, the total radiative rate A_i from the excited state $^5D_4$ is derived from the experimental fluorescence decay time as:

$$A_i = \sum_j \left(A_{i\longrightarrow j}^{ed} + A_{i\longrightarrow j}^{md}\right) = \frac{1}{\tau_{rad}} \quad (7)$$

The electric dipole transition rate $A_{i\longrightarrow j}^{ed}$ is calculated using:

$$A_{i\longrightarrow j}^{ed} = \frac{64\pi^4 e^2 \nu^3 n(n^2+2)^2}{27h(2J+1)} \sum_{\lambda=2,4,6} \Omega_\lambda \left|\langle J||U^{(\lambda)}||J\rangle\right|^2 \quad (8)$$

The magnetic dipole component is evaluated separately, and relevant doubly reduced matrix elements for Tb^{3+} were taken from literature.

To support our analysis and for comparison of the spectral assignment, the conventional Judd–Ofelt framework as presented by Loiko et al. [37] was also referenced. This work emphasizes the spectral sensitivity of Ω_2 and the importance of accurate band resolution. However, in our case, the hypersensitive $^5D_4 \rightarrow {}^7F_2$ transition exhibited very weak intensity and could not be reliably resolved due to potential overlap with neighboring emissions. Therefore, Ω_2 was excluded from the fitting, and only Ω_4 and Ω_6 parameters were evaluated.

The photoluminescence (PL) emission spectrum exhibits a series of sharp f–f transitions assigned to the $^5D_4 \rightarrow {}^7F_J$ (J = 6–0) manifold of the Tb^{3+} ion, with the most intense green emission centered at 542 nm ($^5D_4 \rightarrow {}^7F_5$).

Electric dipole transition probabilities were estimated by numerically integrating the emission intensities of the resolved bands using Gaussian peak fitting.The integrated areas were then used to calculate the experimental oscillator strengths (f_{exp}), which were subsequently converted to electric dipole line strengths (S_{ED}) using the expression provided by Ofelt [38]:

$$f_{exp} = \frac{8\pi^2 m_e c n(n^2+2)^2}{3h(2J+1)\lambda^2} . S_{ED} \quad (9)$$

where m_e is the electron mass, c is the speed of light, h is Planck's constant, and n is the refractive index (estimated as n ≈ 1.67 via the Dimitrov–Sakka model ($n = \left(6\sqrt{5/E_g} - 2\right)^{1/2}$ with an optical band gap of E_g = 2.90 eV) [39], λ denotes the emission wavelength (in cm), and J is the total angular momentum of the initial state (J = 4 for $^5D_4$).

Theoretical electric dipole line strengths (S_{ED}) were calculated using the J-O formalism [38]:

$$S_{ED} = \sum_{\lambda=2,4,6} \Omega_\lambda \langle U^{(\lambda)}\rangle^2 \quad (10)$$

Here, Ω_λ denotes the J-O intensity parameters, and $\langle U^{(\lambda)}\rangle^2$ represents the squared reduced matrix elements for the respective transitions, known for Tb^{3+} and taken from literature.

A least-squares fitting procedure was employed to determine the optimal J-O parameters (Ω_4 and Ω_6) by minimizing the deviation between the experimental and theoretical line strengths. The $^5D_4 \rightarrow {}^7F_6$ transition was included in the analysis using a small electric dipole contribution, as the integrated intensity was experimentally measurable. In contrast, the $^5D_4 \rightarrow {}^7F_2$ transition was not clearly observable in the emission spectrum, likely due to high local symmetry around Tb^{3+} ions, which tends to suppress hypersensitive transitions. Consequently, the Ω_2 parameter was excluded from this analysis. The calculated J-O parameters for $NaGd(BO_2)_4$:0.02 Tb^{3+} are as follows:

- $\Omega_4 = 0.41 \times 10^{-20}$ cm^2
- $\Omega_6 = 0.64 \times 10^{-20}$ cm^2

Table 4
Comparison of the Judd-Ofelt parameters of Tb^{3+} in NGBO and other hosts.

Compounds	Ω_4 (10^{-20} cm^2)	Ω_6 (10^{-20} cm^2)	Ref.
NGBO phosphor	0.41	0.64	This work
$Al_3(BO_3)_4$ crystal	2.41	4.91	Colak and Zwicker [43]
SYT phosphor	0.45	0.72	Wang et al. [42]
LiPbAlB glasses	0.64	0.22	Deopa and A. S. Rao [40]
$K_7SrY_2(B_5O_{10})_3$ phosphor	0.96	1.12	S. Cam Kaynar et al. [11]

These parameters suggest a moderately asymmetric local environment around Tb^{3+} ions, which is consistent with the observed strong electric dipole transitions. Specifically, the Ω_4 and Ω_6 parameters are typically associated with long-range lattice dynamics and structural rigidity of the host matrix [40–42], were found to be of moderate magnitude. This implies that the NGBO host offers a spectroscopically favorable and structurally stable environment for Tb^{3+} emission. Furthermore, using the acquired J-O parameters, the radiative properties of the $^5D_4$ excited state were analyzed. As shown in Table 3, the $^5D_4 \rightarrow {}^7F_5$ transition dominates with a branching ratio of approximately 87.25 %, indicating highly efficient green emission, which is desirable for photonic applications.

All electric dipole transitions, excluding the magnetic-dipole-dominated $^5D_4 \rightarrow {}^7F_6$ transition, were used in the least-squares fitting to extract the Ω_4 and Ω_6 parameters presented in Table 4.

Using the extracted Judd-Ofelt parameters, the radiative transition probabilities (A_r), total radiative rate (ΣA_r), and theoretical radiative lifetime (τ_{rad}) were calculated.

The theoretical lifetime τ_{rad} was calculated using:

$$\tau_{rad} = \frac{1}{\sum A_r} \quad (9)$$

The obtained result, τ_{rad} ≈ 0.973 ms, closely agrees with the experimentally measured lifetime (τ_{exp} ≈ 0.942 ms), confirming both the validity of the analysis and the high radiative efficiency of the $NaGd(BO_2)_4$:Tb^{3+} phosphor.

It is important to note that the Ω_2 parameter, which is typically derived from the hypersensitive $^5D_4 \rightarrow {}^7F_2$ transition, could not be evaluated in this study due to the extremely weak or absent intensity of this transition in the emission spectrum of NGBO:Tb^{3+}. This behaviour is attributed to the relatively high symmetry of the crystal field surrounding the Tb^{3+} ions, which tends to suppress electric-dipole transitions that are hypersensitive to local symmetry perturbations. Such suppression has been previously reported in Tb^{3+}-activated hosts where ions occupy inversion centers or symmetric lattice sites, thereby diminishing the oscillator strength of the $^5D_4 \rightarrow {}^7F_2$ transition [42]. Although Wang et al. were able to determine a small Ω_2 value (0.29×10^{-20} cm^2) for SYT:Tb^{3+}, our system exhibited an even weaker $^5D_4 \rightarrow {}^7F_2$ transition, making the extraction of a reliable Ω_2 parameter infeasible.

As a result, Judd–Ofelt analysis in this work was restricted to the evaluation of Ω_4 and Ω_6 parameters, derived from more intense and symmetry-insensitive transitions. Despite the absence of Ω_2, the calculated radiative lifetime (τ_{rad}) using only Ω_4 and Ω_6 showed good agreement with experimental lifetime values, as discussed later in the manuscript. Similar approaches have been adopted in other studies when the hypersensitive transition could not be resolved with sufficient accuracy. Therefore, the exclusion of Ω_2 does not compromise the validity of the radiative parameters obtained in this work.

Consequently, only Ω_4 and Ω_6 parameters were extracted from the well-resolved electric dipole transitions using the J-O model. Although conservative, this approach yields reliable insights into the radiative

Table 5
Radiative parameters calculated for $^5D_4 \rightarrow {}^7F_a$ transitions in NGBO:Tb^{3+} (2 wt%) based on J-O theory, including squared reduced matrix elements ($\langle U^\lambda \rangle^2$), integrated emission areas, electric- and magnetic-dipole transition probabilities (A_{ed}, A_{md}), total transition rates (A_T), and branching ratios (β).

Transition	$\langle U^\lambda \rangle^2$	Area (a. u.)	A_{ed} (s^{-1})	A_{md} (s^{-1})	A_T (s^{-1})	β (%)
$^5D_4 \rightarrow {}^7F_6$	0.0030 (λ = 2)	35.112	14.2	15.4	29.6	2.61
$^5D_4 \rightarrow {}^7F_5$	0.0032 (λ = 4)	117.401	892.5	0	892.5	78.61
$^5D_4 \rightarrow {}^7F_4$	0.0021 (λ = 6)	66.089	142.3	0	142.3	12.53
$^5D_4 \rightarrow {}^7F_3$	0.0016 (λ = 6)	33.859	71.1	0	71.1	6.26
Total					1135.5	100.00

properties of the system based on dominant electric dipole transitions.

Furthermore, the radiative properties of the $^5D_4$ energy level of Tb^{3+} ions were evaluated using the extracted J-O parameters and are summarized in Table 5. Notably, the $^5D_4 \rightarrow {}^7F_5$ transition exhibits the highest branching ratio (β ≈ 78.61 %), clearly dominating the overall emission profile. This finding underscores the highly efficient green luminescence originating from this electric dipole transition, confirming the favorable spectroscopic environment provided by the NGBO host lattice for Tb^{3+} ions. Moreover, the close agreement between theoretical and experimental lifetimes further validates the reliability of τ_{rad} estimation based solely on Ω_4- and Ω_6-governed transitions, as also supported in previous literature where Ω_2 was omitted under similar conditions.

CIE chromaticity and color tunability via alkali ion Co-Doping

The CIE 1931 chromaticity diagrams of NGBO:$x$$Tb^{3+}$ phosphors and their K^+/Li^+ co-doped counterparts are depicted in Fig. 8. The color coordinates were extracted from photoluminescence emission spectra under 377 nm excitation, and reflect the spectral distribution of the $^5D_4 \rightarrow {}^7F_J$ (J = 6–3) transitions of Tb^{3+} ions.

As illustrated in Fig. 9a, increasing the Tb^{3+} concentration from 0.5 to 7 wt% causes a slight shift of the chromaticity coordinates within the green–blue region. Notably, the sample doped with 2 wt% Tb^{3+} (point C: $x = 0.2728$, $y = 0.3061$) is positioned closest to the white-light region of the diagram, coinciding with the maximum PL intensity reported earlier. This convergence indicates a balanced spectral contribution from the green and blue transitions ($^5D_4 \rightarrow {}^7F_5$ and $^5D_4 \rightarrow {}^7F_6$), rendering this

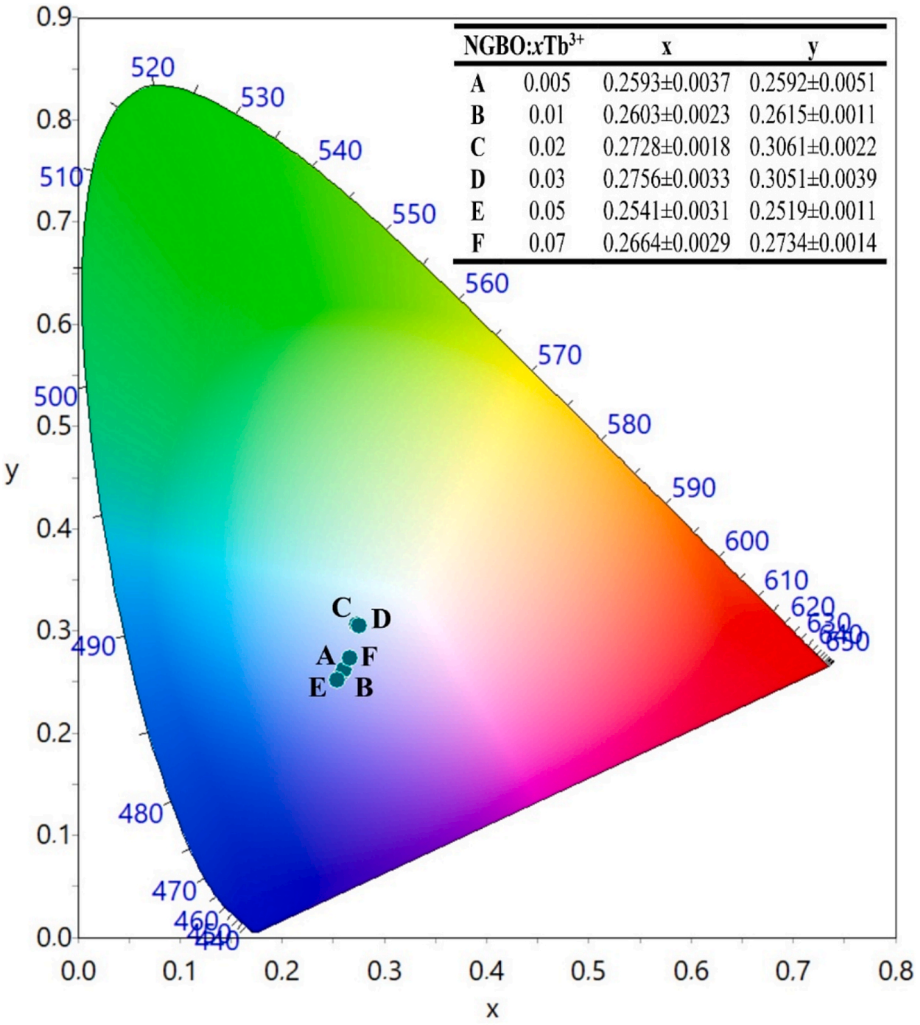

Fig. 9. CIE 1931 chromaticity diagrams for (a) NGBO:x Tb^{3+} (x = 0.005–0.07), (b) NGBO:0.02 Tb^{3+},y K^+, and (c) NGBO:0.02 Tb^{3+},yLi^+ phosphors under 377 nm excitation. The corresponding color coordinates (x, y) are listed in each inset table.

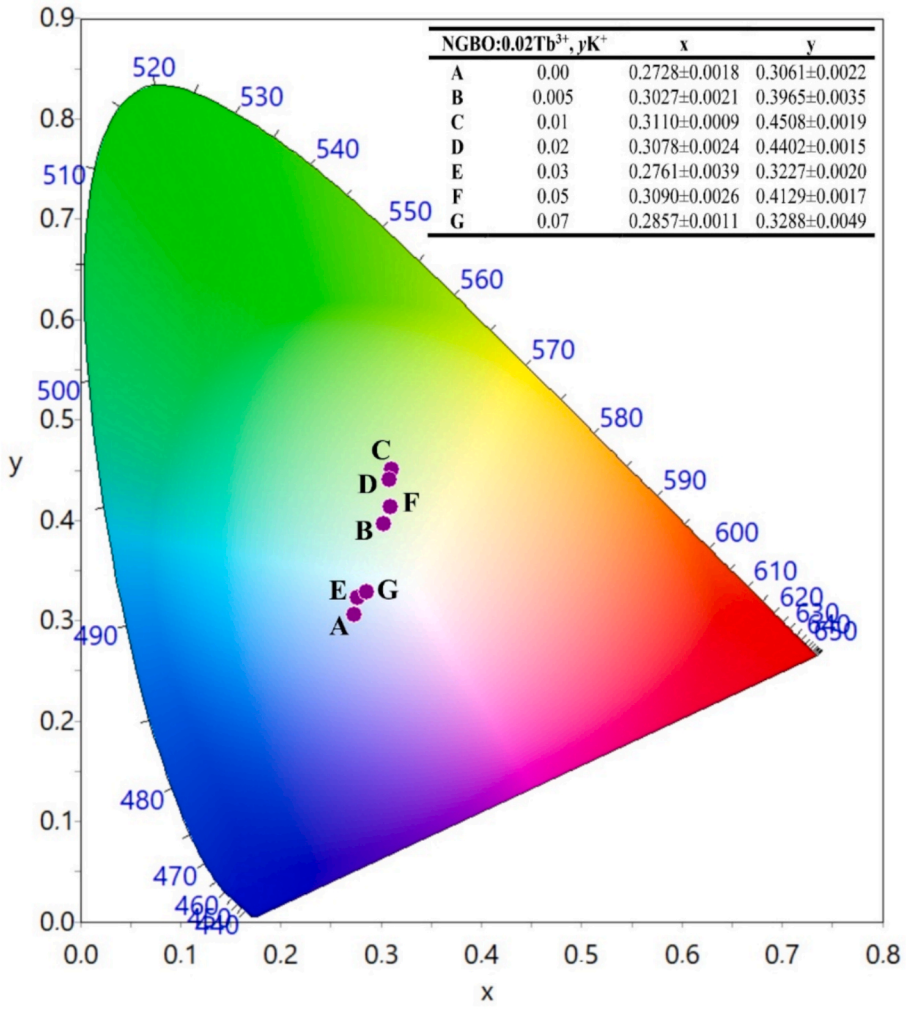

(b)

Fig. 9. (*continued*).

composition highly suitable for white-light emission (WLED) applications.

Upon K^+ co-doping (Fig. 9b), the chromaticity coordinates shift upward and rightward toward the yellow-green region, especially at low to moderate K^+ concentrations (e.g., $y = 0.01$–0.02). This trend is consistent with the enhanced relative intensity of the green emission band and suggests effective modulation of the local crystal field symmetry surrounding Tb^{3+} sites. Interestingly, at higher K^+ concentrations ($y \geq 0.05$), the chromaticity shift slightly reverses, likely due to lattice strain or concentration quenching effects influencing energy transfer dynamics.

In contrast, Li^+ co-doping (Fig. 9c) results in a more gradual and centralized shift of chromaticity coordinates toward the green-white region. The chromaticity point for NGBO:0.02 Tb^{3+},0.05Li^+ (point E: $x = 0.2989$, $y = 0.4398$) is located closest to the pure green zone, confirming the dominance of the $^5D_0 \rightarrow {}^7F_5$ transition. Compared to K^+ co-doping, Li^+ induces less spectral asymmetry, likely owing to its smaller ionic radius and reduced impact on lattice distortion.

Overall, these findings demonstrate that both Tb^{3+} concentration and alkali ion co-doping act as effective tuning parameters for emission color modulation in NGBO phosphors. The ability to tune the emission color from bluish-green to yellowish-green while maintaining high PL intensity underscores the strong potential of these materials for applications in white LEDs, display backlighting, and optical sensing.

To further contextualize the photoluminescence performance of NGBO:Tb^{3+} phosphors, particularly in terms of emission efficiency, chromaticity control, and lifetime behavior, a comparative summary with other Tb^{3+}-activated host materials is presented in Table 6. This benchmarking highlights the relative position of NGBO within the broader spectrum of Tb^{3+}-doped phosphors, demonstrating its competitive or superior optical characteristics for solid-state lighting applications.

Conclusion

In this study, NGBO:Tb^{3+} phosphors were successfully synthesized using a microwave-assisted gel combustion method, and their photoluminescence properties were systematically investigated with emphasis on dopant optimization, co-doping effects, and thermal stability. Under 377 nm excitation, the phosphors exhibited intense green emissions centered at 542 nm ($^5D_4 \rightarrow {}^7F_5$), with the maximum PL intensity observed at 2 wt% Tb^{3+}, indicating optimal luminescent performance prior to concentration quenching. At higher concentration, a classical concentration quenching effect was observed, primarily driven by electric quadrupole–quadrupole interactions, as confirmed by a θ value of approximately 10.11 from Van Uitert analysis. Alkali ion co-doping

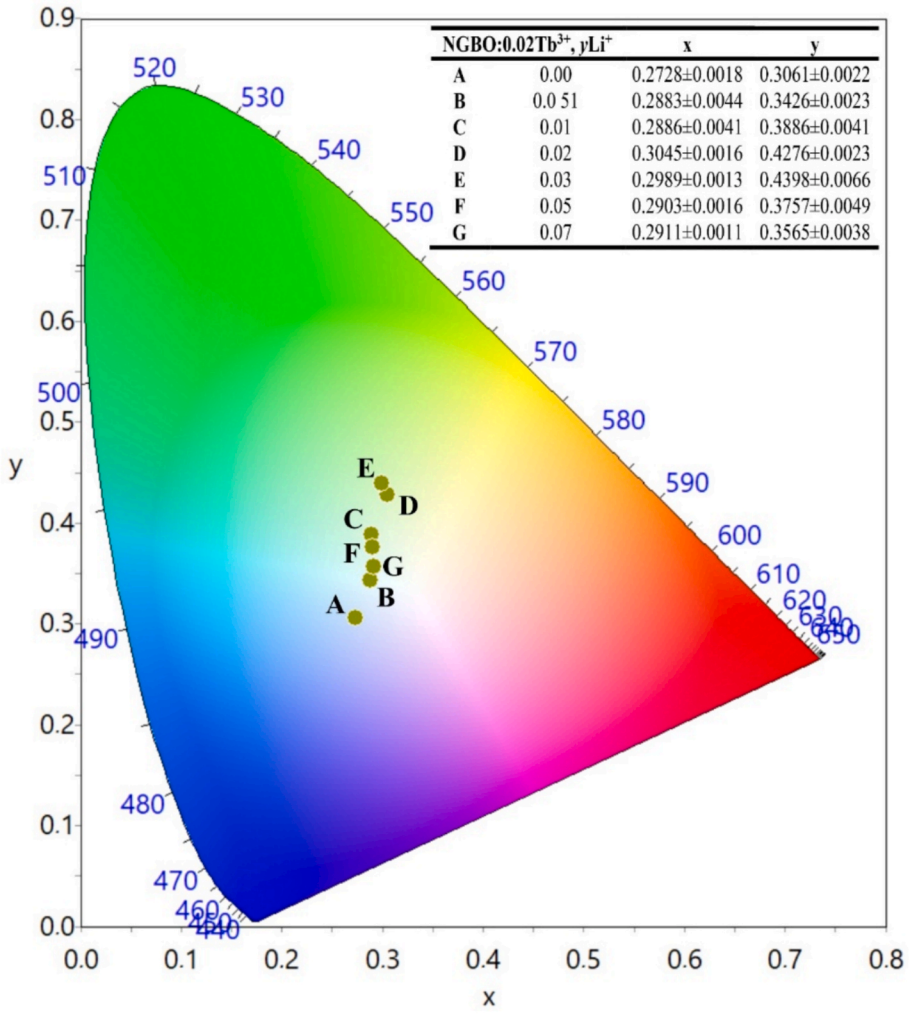

(c)

Fig. 9. (*continued*).

Table 6
Comparative summary of key photoluminescence properties of NGBO:Tb^{3+} and other Tb^{3+}-doped phosphor materials, including emission peak wavelength, average decay lifetime, and CIE chromaticity coordinates under near-UV excitation.

Host material	PL λ_{em} (nm)	τ_{avg} (ms)	CIE (*x*, *y*)	Ref.
NGBO:0.02 Tb^{3+}	542	1.044	(0.272,0.306)	This work
$YBa_3(BO_3)_3$: Tb^{3+}	547	0.949	(0.288,0.430)	Altowyan et al. [44]
$LiMgPO_4$:Tb^{3+}	545	1.120	(0.290, 0.460)	Kati [45]
Sr_2YTaO_6	552	1.370	(0.283, 0.426)	Wang et al.[42]
$KYb(WO_4)_2$	549	0.395	(0.312, 0.644)	Loiko et al.[37]

with K^+ and Li^+ significantly enhanced the PL intensity—by up to 5.33-fold and 3.41-fold, respectively—through lattice distortions, suppressing non-radiative defects, and improvement of the local crystal field environment surrounding Tb^{3+} ions. Time-resolved decay measurements revealed extended average lifetimes, further supporting the suppression of non-radiative quenching pathways. Notably, the co-doped samples exhibited compositional color tunability, with CIE coordinates spanning from bluish-green to yellowish-green. The optimal emission color ($x = 0.2728$, $y = 0.3061$) lies close to the white-light region, highlighting favorable chromatic performance. Additionally, the NGBO:0.02 Tb^{3+} phosphor exhibited rare negative thermal quenching (NTQ) behavior, where emission intensity increased with temperature—attributed to thermally assisted carrier de-trapping and indicating strong thermal robustness. Judd–Ofelt analysis produced radiative parameters ($\Omega_4 = 0.41 \times 10^{20}$ cm^2, $\Omega_6 = 0.64 \times 10^{20}$ cm^2), providing additional insight into electronic transition probabilities and confirming the spectroscopic viability of the host matrix. Furthermore, the demonstrated ability to achieve efficient green emission through direct excitation of Tb^{3+} ions—without employing sensitizer ions—confirms the intrinsic suitability of the NGBO host for rare-earth photonics. This work also represents the first application of Judd–Ofelt theory to Tb^{3+}-doped NGBO phosphors, offering new insights into the correlation between local symmetry and radiative behavior in borate-based systems. Collectively, these findings demonstrate that NGBO:Tb^{3+} phosphors, particularly those co-doped with alkali ions, are highly efficient, thermally stable, and color-tunable, making them strong candidates for green-emitting components in solid-state lighting, optical thermometry, and advanced photonic applications. In future studies, the integration of NGBO:Tb^{3+} phosphors into white LED prototypes or their use in upconversion-based applications may be explored. Additionally, substituting Tb^{3+} with other rare-earth

ions (e.g., Eu^{3+}, Dy^{3+}, or Ce^{3+}) could further tailor the emission characteristics for specific optoelectronic applications.

CRediT authorship contribution statement

G. Souadi: Investigation, Formal analysis. **M.B. Coban:** Investigation, Funding acquisition, Formal analysis. **U.H. Kaynar:** Methodology, Formal analysis. **H. Aydin:** Methodology, Investigation. **S.Cam Kaynar:** Methodology, Investigation. **V. Onar:** Software, Methodology. **A. Canimoglu:** Software, Methodology. **Hussain J Alathlawi:** Software, Methodology. **N. Can:** Writing – review & editing, Writing – original draft, Supervision.

Declaration of competing interest

The authors declare that they have no known competing financial interests or personal relationships that could have appeared to influence the work reported in this paper.

Acknowledgement

The authors gratefully acknowledge the financial support provided by Balıkesir University under BAP Project No. 2024/172.

References

[1] S. Srivastava, S.K. Behera, B.B. Nayak, Opt. Mater. 107 (2020) 110178, https://doi.org/10.1016/j.optmat.2020.110178.
[2] M. Ullah, S.-M. Ban, D.-S. Kim, Opt. Mater. 97 (2019) 109366, https://doi.org/10.1016/j.optmat.2019.109366.
[3] Y. Zhang, L. Li, X. Zhang, D. Wang, S. Zhang, J. Rare Earths 26 (5) (2008) 656–659, https://doi.org/10.1016/S1002-0721(08)60156-8.
[4] Y. Fan, Y. Cao, M. Li, S. Xu, Y. Wang, X. Zhang, J. Zhang, B. Chen, Phys. Chem. Chem. Phys. 26 (46) (2024) 28971–28979, https://doi.org/10.1039/D4CP03989K.
[5] H. Cui, Y. Cao, Y. Zhang, L. Cao, S. Ran, X. Wang, D. Wu, X. Li, X. Zhang, B. Chen, J. Lumin. 241 (2022) 118452, https://doi.org/10.1016/j.jlumin.2021.118484.
[6] C. Guo, H. Jing, T. Li, RSC Adv. 2 (5) (2012) 2119, https://doi.org/10.1039/c2ra00808d.
[7] A. Srivastava, A. Setlur, H. Comanzo, U. Happek, P. Schmidt, ECS Meet. Abstr. MA2005-02(30) (2006) 1117–1117. 10.1149/MA2005-02/30/1117.
[8] T. Sakthivel, L. Sun, B. Devakumar, B. Li, X. Huang, RSC Adv. 8 (57) (2018) 32948–32955, https://doi.org/10.1039/C8RA06607H.
[9] A. George, E. Sreeja, A. Jose, V.K. Vidhu, T. Francis, P.R. Biju, J. Alloys Compd. 1010 (2025) 178177, https://doi.org/10.1016/j.jallcom.2024.178177.
[10] A.B.S. Garcia, A.G. Bispo-Jr, S.A.M. Lima, A.M. Pires, Mater. Res. Bull. 143 (2021) 111462, https://doi.org/10.1016/j.materresbull.2021.111462.
[11] S.C. Kaynar, A.S. Altowyan, H. Aydin, U.H. Kaynar, M.B. Coban, J. Hakami, N. Can, Spectrochim, Acta Part A Mol. Biomol. Spectrosc. 341 (2025) 126435, https://doi.org/10.1016/j.saa.2025.126435.
[12] B.D. Cullity, S.R. Stock, Elements of X-Ray diffraction, Pearson Education Limited, Pearson Education Limited, 2014.
[13] M.K. Alam, M.S. Hossain, N.M. Bahadur, S. Ahmed, J. Mol. Struct. 1306 (2024) 137820, https://doi.org/10.1016/j.molstruc.2024.137820.
[14] W.A. Pisarski, T. Goryczka, B. Wodecka-Duś, M. Płońska, J. Pisarska, Mater. Sci. Eng. B 122 (2) (2005) 94–99, https://doi.org/10.1016/j.mseb.2005.05.002.
[15] C. Gautam, A.K. Yadav, A.K. Singh, ISRN Ceram. 2012 (2012) 1–17, https://doi.org/10.5402/2012/428497.
[16] S. Kuhn, M. Tiegel, A. Herrmann, J. Körner, R. Seifert, F. Yue, D. Klöpfel, J. Hein, M.C. Kaluza, C. Rüssel, Opt. Mater. Express 5 (2) (2015) 430, https://doi.org/10.1364/OME.5.000430.
[17] G. Padmaja, P. Kistaiah, J. Phys. Chem. A 113 (11) (2009) 2397–2404, https://doi.org/10.1021/jp809318e.
[18] L. Song, Y. Wang, A.C. Hannon, S. Feller, W. Li, Y. Zhou, F. Zhu, J. Non. Cryst. Solids 616 (2023) 122478, https://doi.org/10.1016/j.jnoncrysol.2023.122478.
[19] A. Bahadur, R.S. Yadav, R.V. Yadav, S.B. Rai, J. Solid State Chem. 246 (2017) 81–86, https://doi.org/10.1016/j.jssc.2016.11.004.
[20] N. Baig, R.S. Yadav, N.S. Dhoble, V.L. Barai, S.J. Dhoble, J. Lumin. 215 (2019) 116645, https://doi.org/10.1016/j.jlumin.2019.116645.
[21] G. Blasse, Phys. Lett. A 28 (6) (1968) 444–445, https://doi.org/10.1016/0375-9601(68)90486-6.
[22] Y. Zheng, T. Yang, Y. Xiang, K. Xiong, D. Yang, Z. Fang, S. Yang, J. Zhu, J. Alloys Compd. 911 (2022) 165087, https://doi.org/10.1016/j.jallcom.2022.165087.
[23] Y. Xiang, L. Yang, C. Liao, X. Xiang, X. Tang, H. Tang, J. Zhu, J. Adv. Ceram. 12(4) (2023) 848–60. 10.26599/JAC.2023.9220725.
[24] Z. Ghubish, M. El-Kemary, J. Ind. Eng. Chem. 107 (2022) 61–74, https://doi.org/10.1016/j.jiec.2021.11.026.
[25] Y. Tian, B. Chen, B. Tian, R. Hua, J. Sun, L. Cheng, H. Zhong, X. Li, J. Zhang, Y. Zheng, T. Yu, L. Huang, Q. Meng, J. Alloys Compd. 509 (20) (2011) 6096–6101, https://doi.org/10.1016/j.jallcom.2011.03.034.
[26] Z. Wan, D. Xu, W. She, F. Xie, Y. Feng, J. Yang, G. Liu, X. Tong, Ceram. Int. 50 (6) (2024) 9499–9509, https://doi.org/10.1016/j.ceramint.2023.12.268.
[27] B. Zhang, S. Ying, L. Han, J. Zhang, B. Chen, RSC Adv. 8 (45) (2018) 25378–25386, https://doi.org/10.1039/C8RA05515G.
[28] Monika, R.S. Yadav, A. Bahadur, S.B. Rai, RSC Adv. 13(29) (2023) 20164–78. 10.1039/D3RA03215A.
[29] R. Priya, O.P. Pandey, J. Lumin. 212 (2019) 342–353, https://doi.org/10.1016/j.jlumin.2019.04.043.
[30] J. Li, Y. Wang, B. Liu, J. Lumin. 130 (6) (2010) 981–985, https://doi.org/10.1016/j.jlumin.2010.01.009.
[31] S. Som, S.K. Sharma, T. Shripathi, J. Fluoresc. 23 (3) (2013) 439–450, https://doi.org/10.1007/s10895-013-1160-7.
[32] A.S. Altowyan, U.H. Kaynar, H. Aydin, J. Hakami, M.B. Coban, K. Cikrikci, M. Ayvacikli, N. Can, Mater. Sci. Semicond. Process. 195 (2025) 109593, https://doi.org/10.1016/j.mssp.2025.109593.
[33] S. Verma, K. Verma, D. Kumar, B. Chaudhary, S. Som, V. Sharma, V. Kumar, H. C. Swart, Phys. B Condens. Matter 535 (2018) 106–113, https://doi.org/10.1016/j.physb.2017.06.073.
[34] A.P. Shablinskii, O.Y. Shorets, A.V. Povotskiy, R.S. Bubnova, M. G. Krzhizhanovskaya, S.Y. Janson, V.L. Ugolkov, S.K. Filatov, Crystals 14 (12) (2024) 1074, https://doi.org/10.3390/cryst14121074.
[35] M. Luo, B. Chen, X. Li, J. Zhang, S. Xu, X. Zhang, Y. Cao, J. Sun, Y. Zhang, X. Wang, Y. Zhang, D. Gao, L. Wang, Phys. Chem. Chem. Phys. 22 (43) (2020) 25177–25183, https://doi.org/10.1039/D0CP04379F.
[36] Y. Zhang, B. Chen, S. Xu, X. Li, J. Zhang, J. Sun, X. Zhang, H. Xia, R. Hua, Phys. Chem. Chem. Phys. 20 (23) (2018) 15876–15883, https://doi.org/10.1039/C8CP02317D.
[37] P. Loiko, X. Mateos, E. Dunina, A. Kornienko, A. Volokitina, E. Vilejshikova, J. M. Serres, A. Baranov, K. Yumashev, M. Aguiló, F. Díaz, J. Lumin. 190 (2017) 37–44, https://doi.org/10.1016/j.jlumin.2017.05.031.
[38] G.S. Ofelt, J. Chem. Phys. 37 (3) (1962) 511–520, https://doi.org/10.1063/1.1701366.
[39] V. Dimitrov, S. Sakka, J. Appl. Phys. 79 (3) (1996) 1741–1745, https://doi.org/10.1063/1.360963.
[40] N. Deopa, A.S. Rao, J. Lumin. 194 (2018) 56–63, https://doi.org/10.1016/j.jlumin.2017.09.057.
[41] C.R. Kesavulu, A.C. Almeida Silva, M.R. Dousti, N.O. Dantas, A.S.S. de Camargo, T. Catunda, J. Lumin. (2015) 77–84, https://doi.org/10.1016/j.jlumin.2015.04.012.
[42] L. Wang, Y. Zhang, D. Gao, X. Sha, X. Chen, Y. Zhang, J. Zhang, X. Zhang, Y. Cao, Y. Wang, X. Li, S. Xu, H. Yu, B. Chen, Dalt. Trans. 53 (14) (2024) 6399–6409, https://doi.org/10.1039/D4DT00302K.
[43] S. Colak, W.K. Zwicker, J. Appl. Phys. 54 (5) (1983) 2156–2166, https://doi.org/10.1063/1.332393.
[44] A.S. Altowyan, U.H. Kaynar, C. Gök, H. Aydin, J. Hakami, M.B. Coban, A. Canimoglu, N. Can, J. Lumin. 286 (2025) 121380, https://doi.org/10.1016/j.jlumin.2025.121380.
[45] M.İ. Katı, Int. J. Appl. Ceram. Technol. 21 (3) (2024) 2482–2497, https://doi.org/10.1111/ijac.14653.